





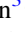




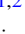







CrossMark

NICER View of the 2020 Burst Storm and Persistent Emission of SGR 1935+2154

George Younes^{1,2} , Tolga Güver^{3,4} , Chryssa Kouveliotou^{1,2} , Matthew G. Baring⁵ , Chin-Ping Hu⁶ ,
Zorawar Wadiasingh⁷ , Beste Begičarslan³ , Teruaki Enoto⁸ , Ersin Göğüş⁹ , Lin Lin¹⁰ , Alice K. Harding⁷ ,
Alexander J. van der Horst^{1,2} , Walid A. Majid^{11,12} , Sebastien Guillot¹³ , and Christian Malacaria^{14,15} 

¹Department of Physics, The George Washington University, Washington, DC 20052, USA; gyounes@gwu.edu

²Astronomy, Physics and Statistics Institute of Sciences (APSYS), The George Washington University, Washington, DC 20052, USA

³Istanbul University, Science Faculty, Department of Astronomy and Space Sciences, Beyazit, 34119, Istanbul, Turkey

⁴Istanbul University Observatory Research and Application Center, Istanbul University 34119, Istanbul, Turkey

⁵Science and Technology Institute, Universities Space Research Association, Huntsville, AL 35805, USA

⁶Department of Physics, National Changhua University of Education, Changhua 50007, Taiwan

⁷Astrophysics Science Division, NASA Goddard Space Flight Center, Greenbelt, MD 20771, USA

⁸Extreme Natural Phenomena RIKEN Hakubi Research Team, Cluster for Pioneering Research, RIKEN, 2-1 Hirosawa, Wako, Saitama 351-0198, Japan

⁹Sabancı University, Faculty of Engineering and Natural Sciences, İstanbul 34956, Turkey

¹⁰Department of Astronomy, Beijing Normal University, Beijing 100875, People's Republic of China

¹¹Jet Propulsion Laboratory, California Institute of Technology, Pasadena, CA 91109, USA

¹²California Institute of Technology, Pasadena, CA 91125, USA

¹³IRAP, CNRS, 9 avenue du Colonel Roche, BP 44346, F-31028 Toulouse Cedex 4, France

¹⁴NASA Marshall Space Flight Center, NSSTC, 320 Sparkman Drive, Huntsville, AL 35805, USA

¹⁵Universities Space Research Association, Science and Technology Institute, 320 Sparkman Drive, Huntsville, AL 35805, USA

Received 2020 September 16; revised 2020 October 27; accepted 2020 November 10; published 2020 November 27

Abstract

We report on NICER observations of the magnetar SGR 1935+2154, covering its 2020 burst storm and long-term persistent emission evolution up to ~ 90 days postoutburst. During the first 1120 s taken on April 28 00:40:58 UTC, we detect over 217 bursts, corresponding to a burst rate of >0.2 bursts s^{-1} . Three hours later, the rate was 0.008 bursts s^{-1} , remaining at a comparatively low level thereafter. The T_{90} burst duration distribution peaks at 840 ms; the distribution of waiting times to the next burst is fit with a lognormal with an average of 2.1 s. The 1–10 keV burst spectra are well fit by a blackbody, with an average temperature and area of $kT = 1.7$ keV and $R^2 = 53$ km². The differential burst fluence distribution over ~ 3 orders of magnitude is well modeled with a power-law form $dN/dF \propto F^{-1.5 \pm 0.1}$. The source persistent emission pulse profile is double-peaked hours after the burst storm. We find that the burst peak arrival times follow a uniform distribution in pulse phase, though the fast radio burst associated with the source aligns in phase with the brighter peak. We measure the source spin-down from heavy-cadence observations covering days 21–39 postoutburst, $\dot{\nu} = -3.72(3) \times 10^{-12}$ Hz s^{-1} , a factor of 2.7 larger than the value measured after the 2014 outburst. Finally, the persistent emission flux and blackbody temperature decrease rapidly in the early stages of the outburst, reaching quiescence 40 days later, while the size of the emitting area remains unchanged.

Unified Astronomy Thesaurus concepts: Neutron stars (1108); Magnetars (992); Soft gamma-ray repeaters (1471)

Supporting material: machine-readable tables

1. Introduction

Large variability patterns over a broad range of timescales (milliseconds to years) is a defining property of magnetars, rarely shared with other classes of the isolated neutron star family. Most common are the short (average duration ~ 200 ms), very bright ($L_X \lesssim 10^{42}$ erg s^{-1}), hard X-ray bursts, ubiquitously detected from the majority of the magnetar population. These bursts can occur in isolation, with a single to a few bursts observed (e.g., An et al. 2015; Younes et al. 2020b), or during a burst storm, when hundreds are detected within hours to days from the start of the source activity (e.g., Israel et al. 2008; van der Horst et al. 2012). The least common form of magnetar bursting activity is the emission of a giant flare (GF). These consist of an initial subsecond hard “spike” reaching luminosities of $\sim 10^{47}$ erg s^{-1} , followed by a softer tail pulsating at the spin period of the source and lasting for several minutes. These events have so far been detected on three occasions from three known magnetars (e.g., Mazets et al. 1979; Hurley et al. 1999; Palmer et al. 2005). On longer timescales, magnetars randomly enter active episodes, usually

associated contemporaneously with bursting activity, where their persistent flux level increases by factors of a few to a thousand, accompanied by spectral and temporal variability. These properties often recover to their preoutburst levels months to years after activity cessation (e.g., Woods et al. 2004; Rea et al. 2013; Scholz et al. 2014; Younes et al. 2017a; Coti Zelati et al. 2018). Magnetars are widely believed to be powered by the decay of their supercritical external magnetic fields, often in excess of 10^{14} G (Kouveliotou et al. 1998), and perhaps larger internal ones (Thompson & Duncan 1996; see also Turolla et al. 2015; Kaspi & Beloborodov 2017 for reviews).

In 2014, SGR 1935+2154 was discovered when Swift-BAT triggered on magnetar-like bursts from the Galactic plane direction (Stamatikos et al. 2014), close to the geometrical center of the supernova remnant G57.2+0.8 (Kothes et al. 2018). Subsequent Chandra and XMM-Newton monitoring revealed a source spin period of $P = 3.24$ s and a spin-down rate of $\dot{P} = 1.43 \times 10^{-11}$ s s^{-1} , implying a magnetar-like dipolar B -field strength, $B \approx 2.2 \times 10^{14}$ G, at the equator, which, together with the bursts, cemented its identification as a

magnetar source (Israel et al. 2016). Since its discovery, SGR 1935+2154 has been very active, showing outbursts in 2015 and 2016, each more intense than the preceding one in terms of total number of bursts per active episode, total energy emitted in bursts, and persistent emission from the source (Younes et al. 2017b; Lin et al. 2020).

On 2020 April 27, a multitude of wide field-of-view instruments detected intense bursting activity from SGR 1935+2154, comprising its most prolific episode since discovery (Fletcher & Fermi GBM Team 2020; Palmer 2020; Younes et al. 2020c). Hours after the initial trigger, an intense radio burst from the direction of SGR 1935+2154 was independently detected with the Canadian Hydrogen Intensity Mapping Experiment (CHIME; CHIME/FRB Collaboration et al. 2020) and the Survey for Transient Astronomical Radio Emission 2 (STARE2; Bochenek et al. 2020) radio telescopes at 400–800 MHz and 1.4 GHz, respectively. This radio burst had a fluence of the order of 1 MJy ms, bright enough to be potentially detectable at distances of several tens of megaparsecs by existing large radio facilities (Bochenek et al. 2020); this places it close to the faint end of the extragalactic fast radio burst (FRB) population. Simultaneous to the radio burst, multiple hard X-ray telescopes detected a magnetar-like burst from SGR 1935+2154, with a spectrum somewhat harder than previously observed from the source (Li et al. 2020; Mereghetti et al. 2020; Ridnaia et al. 2020; Tavani et al. 2020). This exceptional FRB–X-ray burst association placed magnetars at center stage as the potential origin of at least some extragalactic FRBs. Interestingly, SGR 1935+2154 has since shown several millisecond radio bursts with fluences between 3 and 7 orders of magnitude smaller than the FRB-like burst (Good & Chime/Frb Collaboration 2020; Kirsten et al. 2020; Pleunis & CHIME/FRB Collaboration 2020; Zhang et al. 2020; Zhu et al. 2020).

Here we report on the burst storm of SGR 1935+2154 as observed with NICER hours after the activity onset, as well as the ensuing outburst evolution of the source persistent emission. Section 2 summarizes the observations and data reduction. Section 3 presents the temporal and spectral analyses of the burst storm, while Section 4 discusses the analysis of the persistent emission up to 90 days following the outburst onset. We discuss our findings in Section 5.

Throughout the paper, we adopt a fiducial distance toward SGR 1935+2154 of 9 kpc due to the large uncertainties in its distance estimate (Kothes et al. 2018; Mereghetti et al. 2020; Zhong et al. 2020; Zhou et al. 2020).

2. Observations and Data Reduction

NICER is a nonimaging X-ray timing and spectral instrument providing a collecting area of 1900 cm² at 1.5 keV. It consists of 56 coaligned X-ray-concentrating optics covering a (30')² field of view (Gendreau et al. 2016), 52 of which are currently operating. We utilize all 52 detectors for our burst analyses. NICER started observing SGR 1935+2154 on 2020 April 28 at 00:40:58 UTC, 6 hr after the initial Swift-BAT and Fermi-GBM triggers that signaled the start of another burst active period from the source and just under 14 hr prior to the FRB (Barthelmy et al. 2020; Fletcher & Fermi GBM Team 2020). The first observation, with ID 3020560101, had an exposure of 3.1 ks spread over a large portion of April 28. We show the 1–10 keV light curve at 64 ms resolution in the top panel of Figure 1. The first uninterrupted good time interval

(GTI), shown in the middle panel of Figure 1 and totaling 1120 s, caught the tail end of the burst storm from the source. We focus on this observation, and more specifically on the first GTI, for the analysis of the burst forest. For the outburst evolution, however, we analyze all publicly available NICER observations, as summarized in Table 1.

We processed the NICER data using NICERDAS version 7a as part of HEASOFT version 6.27.2. We start our data reduction from level 1 event files. We create GTIs using standard filtering criteria as described in the NICER Data Analysis Guide.¹⁶ Due to the relatively large absorbing hydrogen column density in the direction of SGR 1935+2154 and the reduced NICER sensitivity at high energies, we only consider photons in the energy range 1–10 keV for our temporal and spectral analyses. For the analysis of the bursts, we correct for the loss of exposure fraction due to dead time following the steps described in Younes et al. (2020a). We use the response matrices and ancillary files given in the latest NICER calibration files, version 20200722. The background is estimated from a 40 s long interval centered on each burst peak time after excluding all identified bursts (Figure 1, bottom panel). As for the persistent emission, we estimate the background using the NICER tool `nibackgen3C50`.¹⁷ A bright dust-scattering halo was detected in Swift-XRT on April 27, which decayed very rapidly to almost background level on April 28 (Mereghetti et al. 2020, their Figure 5). Hence, this halo emission may marginally contribute to the sky background, especially during the first GTI of our first NICER observation (Figure 1), which we only use to analyze the bursts. This excess emission is automatically accounted for because it is part of the background of each burst as defined above.

We use XSPEC version 12.11.0k (Arnaud 1996) to perform all spectral analyses. For the burst spectral analysis, we group the spectra to have five counts per energy bin and use the *W*-statistic (command `statistic Cstat` in XSPEC) for model parameter estimation and error calculation. For the persistent emission spectra, we group each spectrum to have at least 50 counts per energy channel for the use of the χ^2 statistics. We use the Tübingen–Boulder model (`tbabs`) to account for interstellar absorption in the direction of SGR 1935+2154, along with the abundances of Wilms et al. (2000) and the photoelectric cross sections of Verner et al. (1996). We report all parameter uncertainties at the 1σ level, unless quoted otherwise.

3. Results

3.1. Burst Identification

We apply a Poissonian procedure to identify bursts within each GTI, starting with dividing it into multiple 100 s duration time intervals, ΔT (e.g., Gavriil et al. 2004). We then create a light curve with 4 ms resolution within each ΔT , resulting in a total of $N = 25,000$ bins interval⁻¹. Next, we calculate the probability P_i of the total counts in each 4 ms time bin, n_i , to be a random fluctuation around the average λ (the ratio of the total counts within ΔT over ΔT) as $P_i = (\lambda^{n_i} \exp(-\lambda))/n_i!$. Any time bin satisfying the criterion $P_i < 0.01/N$ is flagged as part of a burst. The procedure is reiterated until no more bins are

¹⁶ https://heasarc.gsfc.nasa.gov/docs/nicer/data_analysis/nicer_analysis_guide.html

¹⁷ https://heasarc.gsfc.nasa.gov/docs/nicer/tools/nicer_bkg_est_tools.html

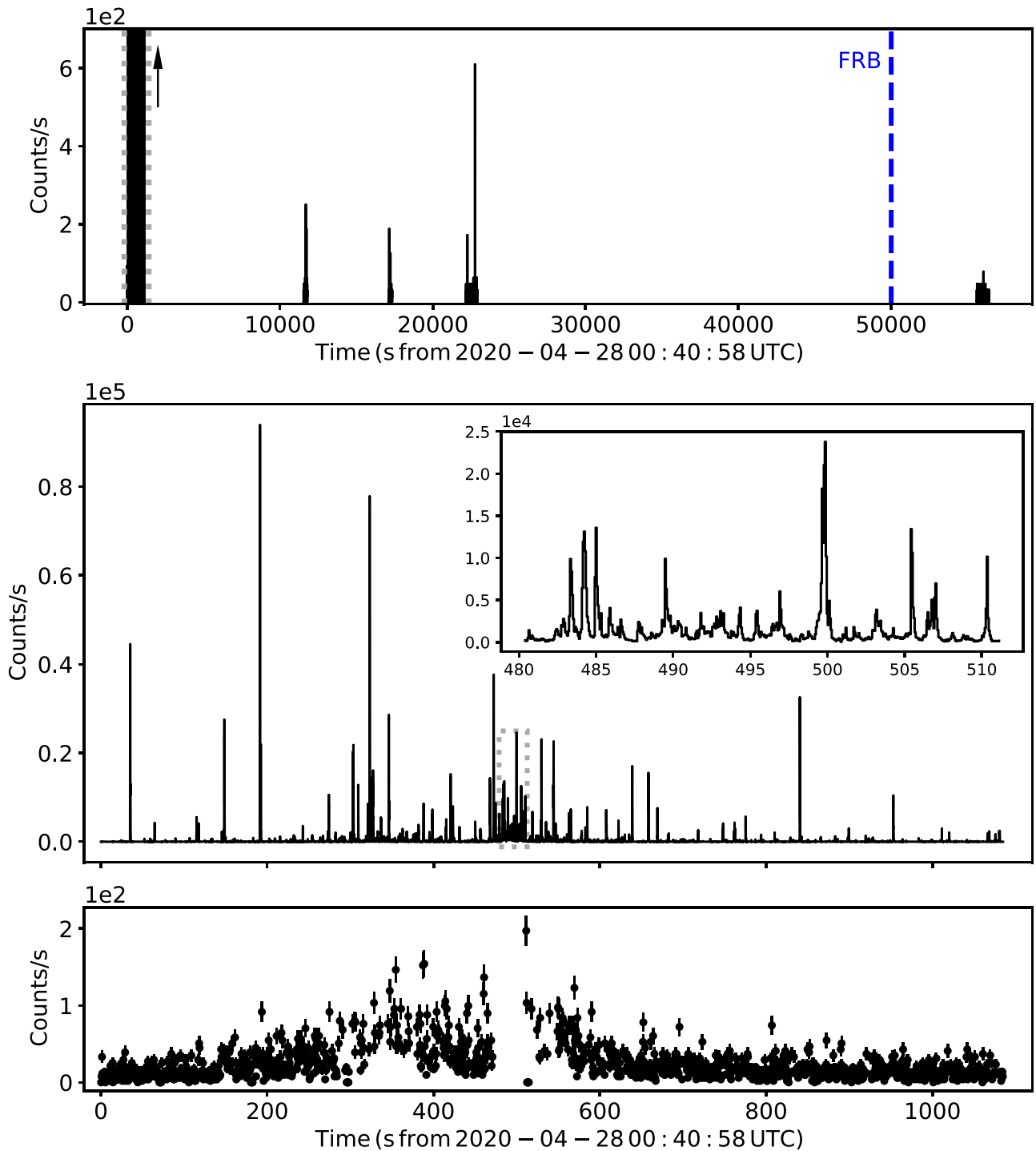


Figure 1. Top panel: NICER light curve of ObsID 3020560101 shown at 64 ms resolution in the 1–10 keV energy range. The blue dashed vertical line is the time of FRB 200428. The gray dashed vertical lines delimit the first GTI when the burst forest occurred. The arrow indicates that the count rate is outside the y-axis limit. Middle panel: “zoom-in” view of the burst forest. We detect more than 217 bursts during ~ 1120 s. The inset is a zoom-in of the area delimited with a dotted gray box, representing the most intense bursting period. Bottom panel: light curve (with 0.5 s resolution) of the burst forest after eliminating all identified bursts.

identified in a ΔT . To capture the weaker tails of bursts, as well as fainter bursts that are not resolved at high resolution, we repeat the above procedure using time resolutions of 32, 128, and 512 ms after excluding all flagged bins of 4 ms, as discussed above. We note that at lower resolutions, the most intense parts of the burst forest, i.e., between 300 and 600 s after the start of the observation (Figure 1, bottom panel), appear to be sitting on a bed of elevated emission. We correct for this variable background by fitting a nonparametric function

to local minima within each ΔT (Eilers & Boelens 2005). We repeat our burst search algorithm for different ΔT , ranging from 20 to 200 s in steps of 20 s. We find that our search algorithm is only weakly dependent on the interval duration.

We define the start of a new burst to be when the emission of the previous burst drops and remains at the background level, after subtracting the elevated emission level, for 0.5 s (i.e., 15% of the source spin period). This establishes a T_{start} and T_{end} for each burst and provides enough background before and after to

Table 1
Spectral Properties of the Persistent Emission

ObsID	MJD ^a (days)	Exposure (s)	Count Rate (counts s ⁻¹)	kT (keV)	Flux ^b	Radius (km)
3020560101	58,967.165	233.70	2.74 ± 0.12	0.79 ^{+0.04} _{-0.04}	2.2 ^{+0.1} _{-0.1}	2.1 ^{+0.2} _{-0.2}
3020560101	58,967.229	231.10	2.16 ± 0.11	0.73 ^{+0.04} _{-0.04}	1.7 ^{+0.1} _{-0.1}	2.2 ^{+0.2} _{-0.2}
3020560101	58,967.293	727.80	1.99 ± 0.06	0.78 ^{+0.03} _{-0.02}	1.54 ^{+0.05} _{-0.05}	1.8 ^{+0.1} _{-0.1}
3020560101	58,967.681	805.90	1.33 ± 0.05	0.65 ^{+0.02} _{-0.02}	0.98 ^{+0.04} _{-0.04}	2.1 ^{+0.2} _{-0.1}
3020560102	58,968.583	934.09	0.95 ± 0.04	0.62 ^{+0.03} _{-0.02}	0.68 ^{+0.03} _{-0.03}	1.9 ^{+0.2} _{-0.1}
3020560103	58,969.551	712.07	0.68 ± 0.04	0.51 ^{+0.03} _{-0.02}	0.51 ^{+0.03} _{-0.03}	2.4 ^{+0.3} _{-0.3}
3020560104	58,980.615	944.04	0.55 ± 0.03	0.47 ^{+0.02} _{-0.02}	0.44 ^{+0.02} _{-0.02}	2.7 ^{+0.3} _{-0.3}
3020560105	58,988.922	915.07	0.46 ± 0.03	0.49 ^{+0.03} _{-0.03}	0.37 ^{+0.02} _{-0.02}	2.2 ^{+0.3} _{-0.3}
3020560106	58,989.589	624.02	0.54 ± 0.03	0.49 ^{+0.03} _{-0.03}	0.40 ^{+0.03} _{-0.03}	2.4 ^{+0.3} _{-0.3}
3020560107	58,991.075	5176.37	0.46 ± 0.01	0.49 ^{+0.01} _{-0.01}	0.34 ^{+0.01} _{-0.01}	2.2 ^{+0.1} _{-0.1}
3020560108	58,992.032	3208.26	0.57 ± 0.02	0.47 ^{+0.02} _{-0.02}	0.40 ^{+0.01} _{-0.01}	2.5 ^{+0.2} _{-0.2}
3020560109	58,994.601	790.06	0.49 ± 0.03	0.52 ^{+0.03} _{-0.03}	0.38 ^{+0.02} _{-0.02}	2.0 ^{+0.3} _{-0.3}
3020560110	58,997.896	1678.12	0.31 ± 0.02	0.40 ^{+0.02} _{-0.02}	0.28 ^{+0.02} _{-0.02}	2.9 ^{+0.4} _{-0.3}
3020560111	58,998.150	963.07	0.34 ± 0.03	0.47 ^{+0.03} _{-0.03}	0.28 ^{+0.02} _{-0.02}	2.1 ^{+0.3} _{-0.3}
3020560112	58,999.249	1279.09	0.41 ± 0.03	0.50 ^{+0.03} _{-0.03}	0.31 ^{+0.02} _{-0.02}	2.0 ^{+0.3} _{-0.3}
3020560114	59,001.130	2745.16	0.46 ± 0.02	0.52 ^{+0.02} _{-0.02}	0.34 ^{+0.01} _{-0.01}	1.9 ^{+0.2} _{-0.2}
3020560115	59,002.992	972.06	0.33 ± 0.03	0.54 ^{+0.04} _{-0.04}	0.26 ^{+0.02} _{-0.02}	1.5 ^{+0.3} _{-0.2}
3020560116	59,003.184	665.04	0.33 ± 0.03	0.47 ^{+0.04} _{-0.04}	0.27 ^{+0.03} _{-0.03}	2.1 ^{+0.4} _{-0.4}
3020560117	59,004.545	1368.08	0.26 ± 0.02	0.48 ^{+0.03} _{-0.03}	0.21 ^{+0.02} _{-0.02}	1.8 ^{+0.3} _{-0.2}
3020560118	59,005.189	1201.07	0.24 ± 0.02	0.44 ^{+0.03} _{-0.03}	0.20 ^{+0.02} _{-0.02}	2.1 ^{+0.3} _{-0.3}
3020560119	59,006.222	990.06	0.19 ± 0.02	0.44 ^{+0.04} _{-0.04}	0.17 ^{+0.02} _{-0.02}	1.9 ^{+0.4} _{-0.3}
3020560120	59,020.891	883.04	0.37 ± 0.03	0.44 ^{+0.03} _{-0.03}	0.31 ^{+0.02} _{-0.02}	2.5 ^{+0.4} _{-0.4}
3020560121	59,021.014	846.04	0.27 ± 0.03	0.37 ^{+0.03} _{-0.03}	0.28 ^{+0.03} _{-0.03}	3.5 ^{+0.8} _{-0.6}
3020560122	59,022.445	1675.05	0.36 ± 0.02	0.41 ^{+0.02} _{-0.02}	0.30 ^{+0.02} _{-0.02}	2.8 ^{+0.3} _{-0.3}
3020560123	59,023.101	3182.09	0.21 ± 0.01	0.42 ^{+0.02} _{-0.02}	0.20 ^{+0.01} _{-0.01}	2.3 ^{+0.2} _{-0.2}
3020560124	59,024.961	1840.05	0.27 ± 0.02	0.44 ^{+0.02} _{-0.02}	0.22 ^{+0.01} _{-0.01}	2.1 ^{+0.3} _{-0.3}
3020560125	59,025.931	1655.04	0.26 ± 0.02	0.43 ^{+0.02} _{-0.02}	0.23 ^{+0.02} _{-0.02}	2.3 ^{+0.3} _{-0.3}
3020560126	59,027.614	847.01	0.29 ± 0.03	0.42 ^{+0.04} _{-0.04}	0.24 ^{+0.03} _{-0.03}	2.6 ^{+0.7} _{-0.5}
3020560127	59,028.705	1703.04	0.15 ± 0.02	0.42 ^{+0.03} _{-0.03}	0.15 ^{+0.02} _{-0.02}	2.0 ^{+0.3} _{-0.3}
3020560128	59,029.802	1692.03	0.20 ± 0.02	0.42 ^{+0.03} _{-0.03}	0.18 ^{+0.02} _{-0.02}	2.2 ^{+0.4} _{-0.3}
3020560129	59,030.699	2150.65	0.21 ± 0.02	0.43 ^{+0.02} _{-0.02}	0.19 ^{+0.01} _{-0.01}	2.1 ^{+0.3} _{-0.3}
3020560130	59,031.529	615.03	0.33 ± 0.04	0.45 ^{+0.04} _{-0.04}	0.27 ^{+0.03} _{-0.03}	2.3 ^{+0.6} _{-0.5}
3020560131	59,032.500	1190.05	0.16 ± 0.02	0.39 ^{+0.03} _{-0.03}	0.19 ^{+0.02} _{-0.02}	2.6 ^{+0.5} _{-0.4}
3020560132	59,033.598	1058.04	0.27 ± 0.02	0.38 ^{+0.03} _{-0.02}	0.26 ^{+0.03} _{-0.02}	3.2 ^{+0.6} _{-0.5}
3020560133	59,034.824	819.03	0.22 ± 0.02	0.40 ^{+0.04} _{-0.04}	0.21 ^{+0.03} _{-0.03}	2.6 ^{+0.7} _{-0.5}
3020560134	59,038.773	496.00	0.13 ± 0.04	0.36 ^{+0.08} _{-0.06}	0.15 ^{+0.05} _{-0.04}	3 ⁺¹ ₋₁
3020560135	59,040.246	361.01	0.19 ± 0.03	0.34 ^{+0.05} _{-0.05}	0.28 ^{+0.10} _{-0.06}	4 ⁺³ ₋₂
3020560136	59,041.431	1267.99	0.24 ± 0.02	0.41 ^{+0.03} _{-0.03}	0.22 ^{+0.02} _{-0.02}	2.4 ^{+0.4} _{-0.4}
3020560137	59,042.848	657.00	0.14 ± 0.03	0.42 ^{+0.05} _{-0.05}	0.14 ^{+0.02} _{-0.02}	1.9 ^{+0.6} _{-0.5}
3020560138	59,045.692	3128.00	0.12 ± 0.02	0.42 ^{+0.02} _{-0.02}	0.14 ^{+0.01} _{-0.01}	1.9 ^{+0.2} _{-0.2}
3020560139	59,046.269	1423.99	0.21 ± 0.02	0.39 ^{+0.03} _{-0.03}	0.21 ^{+0.02} _{-0.02}	2.8 ^{+0.5} _{-0.4}
3020560141	59,049.029	776.01	0.39 ± 0.03	0.39 ^{+0.02} _{-0.02}	0.36 ^{+0.03} _{-0.03}	3.6 ^{+0.6} _{-0.5}
3020560142	59,056.062	222.00	0.42 ± 0.07	0.5 ^{+0.1} _{-0.1}	0.34 ^{+0.07} _{-0.06}	2.0 ⁺² _{-0.8}

Notes.^a Times are given as the middle of each observation.^b The 0.3–10 keV flux values are unabsorbed and in units of $\times 10^{-11}$ erg s⁻¹ cm⁻².

(This table is available in machine-readable form.)

derive the burst temporal properties. We identify a total of 217 bursts within the first GTI. At the peak of the burst forest, we identify a 31 s interval (about 10 rotational periods) where the emission never reaches the background level (designated as burst 100 in Table 2). This is shown in the inset of the middle panel of Figure 1. The length of this bursting interval, which contains many individual bursts, is >6 times the duration of the second-longest burst. We exclude this interval from all burst

analyses. In the remaining four GTIs, we identify a total of six bursts.

3.2. Burst Temporal Results

To derive burst temporal properties, we consider the 1–10 keV unbinned events within the interval T_{start} and T_{end} for each burst as estimated above, as well as a background

Table 2
Burst Properties

Burst No.	$T_{st,100}$ (UTC)	$T_{et,100}$ (UTC)	T_{peak} (UTC)	T_{90} (s)	kT (keV)	R^2 (km ²)	$\log_{10} F$ (erg cm ⁻² s ⁻¹)
1	00:41:21.230	00:41:21.479	00:41:21.260	0.194	3^{+5}_{-1}	6^{+10}_{-6}	$-8.5^{+0.2}_{-0.2}$
2	00:41:23.627	00:41:23.759	00:41:23.653	0.088
3	00:41:31.809	00:41:33.964	00:41:32.220	0.41	$3.9^{+0.2}_{-0.2}$	600^{+50}_{-40}	$-6.26^{+0.01}_{-0.01}$
4	00:41:49.245	00:41:49.748	00:41:49.321	0.216	$1.9^{+0.6}_{-0.4}$	30^{+21}_{-13}	$-8.4^{+0.1}_{-0.1}$
5	00:41:53.301	00:41:53.369	00:41:53.367	0.067
6	00:41:56.315	00:41:58.098	00:41:56.329	1.453	$1.7^{+0.2}_{-0.2}$	15^{+5}_{-4}	$-8.81^{+0.05}_{-0.05}$
7	00:42:00.202	00:42:00.482	00:42:00.253	0.225	2^{+2}_{-1}	8^{+14}_{-6}	$-8.8^{+0.2}_{-0.2}$
8	00:42:01.469	00:42:02.506	00:42:01.643	0.538	$2.2^{+0.1}_{-0.1}$	120^{+17}_{-16}	$-7.61^{+0.02}_{-0.02}$
9	00:42:14.191	00:42:14.793	00:42:14.484	0.462	$1.4^{+0.2}_{-0.2}$	60^{+25}_{-18}	$-8.54^{+0.06}_{-0.06}$
10	00:42:26.726	00:42:27.232	00:42:26.739	0.47	$1.2^{+0.3}_{-0.2}$	32^{+23}_{-14}	$-9.0^{+0.1}_{-0.1}$
11	00:42:43.612	00:42:43.976	00:42:43.711	0.188	$2.1^{+0.6}_{-0.4}$	35^{+22}_{-15}	$-8.19^{+0.09}_{-0.09}$
12	00:42:48.123	00:42:48.455	00:42:48.218	0.249	$1.0^{+0.2}_{-0.2}$	94^{+93}_{-48}	$-9.0^{+0.1}_{-0.1}$
13	00:42:51.848	00:42:53.764	00:42:52.058	0.985	$1.96^{+0.08}_{-0.08}$	140^{+15}_{-14}	$-7.68^{+0.02}_{-0.02}$
14	00:42:54.408	00:42:54.866	00:42:54.467	0.274	$2.7^{+0.2}_{-0.2}$	165^{+25}_{-23}	$-7.2^{+0.02}_{-0.02}$
15	00:43:01.767	00:43:03.795	00:43:01.939	1.521	$2.3^{+0.7}_{-0.4}$	5^{+3}_{-2}	$-8.93^{+0.09}_{-0.09}$
16	00:43:09.236	00:43:11.608	00:43:10.976	1.923	$1.7^{+0.2}_{-0.1}$	20^{+5}_{-4}	$-8.72^{+0.04}_{-0.04}$
17	00:43:16.781	00:43:17.206	00:43:16.911	0.331
18	00:43:22.462	00:43:24.047	00:43:22.492	1.401	$1.7^{+0.1}_{-0.1}$	37^{+8}_{-7}	$-8.44^{+0.04}_{-0.03}$
19	00:43:24.684	00:43:26.995	00:43:25.364	0.773	$3.03^{+0.07}_{-0.07}$	470^{+23}_{-22}	$-6.62^{+0.01}_{-0.01}$
20	00:43:33.269	00:43:34.182	00:43:33.334	0.809	$1.2^{+0.2}_{-0.2}$	31^{+21}_{-13}	$-9.13^{+0.09}_{-0.08}$
21	00:43:35.328	00:43:38.004	00:43:37.945	2.015	$1.8^{+0.2}_{-0.1}$	19^{+5}_{-4}	$-8.69^{+0.04}_{-0.04}$
22	00:43:40.402	00:43:40.590	00:43:40.490	0.113	$1.4^{+0.6}_{-0.3}$	52^{+68}_{-33}	$-8.7^{+0.2}_{-0.2}$
23	00:43:42.160	00:43:42.448	00:43:42.183	0.146
24	00:43:44.976	00:43:45.851	00:43:45.240	0.809	$1.7^{+0.3}_{-0.2}$	20^{+9}_{-7}	$-8.68^{+0.07}_{-0.07}$
25	00:44:00.064	00:44:01.836	00:44:00.180	1.366	$1.7^{+0.2}_{-0.2}$	18^{+6}_{-5}	$-8.78^{+0.06}_{-0.06}$
26	00:44:05.033	00:44:05.392	00:44:05.104	0.319	$1.7^{+0.5}_{-0.3}$	20^{+16}_{-10}	$-8.7^{+0.1}_{-0.1}$
27	00:44:08.027	00:44:10.291	00:44:08.368	1.207	$3.40^{+0.07}_{-0.07}$	470^{+17}_{-17}	$-6.5^{+0.01}_{-0.01}$
28	00:44:19.561	00:44:21.128	00:44:19.570	1.433	$1.8^{+0.2}_{-0.2}$	18^{+6}_{-5}	$-8.71^{+0.05}_{-0.05}$
29	00:44:25.351	00:44:27.499	00:44:26.236	0.955	$1.6^{+0.2}_{-0.2}$	34^{+10}_{-8}	$-8.56^{+0.05}_{-0.05}$
30	00:44:31.343	00:44:32.824	00:44:32.458	1.174	$1.7^{+0.2}_{-0.2}$	27^{+8}_{-7}	$-8.63^{+0.05}_{-0.05}$
31	00:44:39.437	00:44:40.107	00:44:40.056	0.417	$1.47^{+0.52}_{-0.3}$	25^{+21}_{-13}	$-8.8^{+0.1}_{-0.1}$
32	00:44:45.119	00:44:45.796	00:44:45.286	0.398	$1.4^{+0.2}_{-0.1}$	77^{+29}_{-22}	$-8.47^{+0.06}_{-0.06}$
33	00:44:48.153	00:44:49.369	00:44:48.974	1.041	$1.7^{+0.2}_{-0.1}$	40^{+10}_{-8}	$-8.42^{+0.04}_{-0.04}$
34	00:44:49.830	00:44:50.063	00:44:49.855	0.123	$1.8^{+0.3}_{-0.2}$	120^{+54}_{-39}	$-7.85^{+0.07}_{-0.07}$
35	00:44:51.116	00:44:52.185	00:44:51.209	0.954	$1.6^{+0.3}_{-0.2}$	14^{+9}_{-6}	$-9.0^{+0.1}_{-0.1}$
36	00:44:55.529	00:44:56.708	00:44:56.358	0.998	$1.9^{+0.4}_{-0.3}$	10^{+5}_{-4}	$-8.88^{+0.08}_{-0.08}$
37	00:44:59.515	00:45:00.664	00:44:59.898	0.3	$2.1^{+0.2}_{-0.1}$	140^{+27}_{-24}	$-7.6^{+0.03}_{-0.03}$
38	00:45:05.650	00:45:06.117	00:45:05.783	0.35	$1.7^{+0.3}_{-0.2}$	44^{+21}_{-15}	$-8.4^{+0.08}_{-0.07}$
39	00:45:09.942	00:45:11.478	00:45:11.175	0.854	$2.0^{+0.1}_{-0.1}$	55^{+10}_{-9}	$-8.07^{+0.03}_{-0.03}$
40	00:45:11.925	00:45:12.400	00:45:12.122	0.365	$1.7^{+0.3}_{-0.2}$	42^{+20}_{-14}	$-8.42^{+0.07}_{-0.07}$
41	00:45:20.704	00:45:20.911	00:45:20.845	0.145
42	00:45:21.060	00:45:22.732	00:45:21.543	1.259	$1.5^{+0.1}_{-0.1}$	43^{+11}_{-9}	$-8.61^{+0.04}_{-0.04}$
43	00:45:23.520	00:45:24.854	00:45:24.151	1.131	$1.6^{+0.2}_{-0.1}$	38^{+10}_{-8}	$-8.51^{+0.04}_{-0.04}$
44	00:45:28.567	00:45:29.696	00:45:28.849	0.915	$1.5^{+0.2}_{-0.2}$	32^{+12}_{-9}	$-8.67^{+0.06}_{-0.06}$
45	00:45:30.111	00:45:31.608	00:45:31.186	1.241	$2.7^{+0.1}_{-0.1}$	79^{+8}_{-7}	$-7.53^{+0.02}_{-0.02}$
46	00:45:33.014	00:45:34.145	00:45:33.729	0.921	$2.0^{+0.9}_{-0.5}$	8^{+7}_{-4}	$-8.9^{+0.1}_{-0.1}$
47	00:45:38.496	00:45:39.493	00:45:39.254	0.655	$2.4^{+0.2}_{-0.2}$	59^{+11}_{-9}	$-7.81^{+0.03}_{-0.03}$
48	00:45:41.129	00:45:42.806	00:45:42.233	1.484	$1.1^{+0.1}_{-0.1}$	37^{+15}_{-11}	$-9.09^{+0.06}_{-0.06}$
49	00:45:43.812	00:45:44.098	00:45:43.978	0.259	$1.7^{+0.3}_{-0.2}$	62^{+26}_{-19}	$-8.24^{+0.07}_{-0.06}$
50	00:45:44.961	00:45:47.429	00:45:46.842	2.015	$1.8^{+0.1}_{-0.1}$	48^{+7}_{-6}	$-8.3^{+0.03}_{-0.03}$
51	00:45:48.375	00:45:49.323	00:45:48.460	0.777	$1.5^{+0.3}_{-0.2}$	23^{+12}_{-8}	$-8.9^{+0.08}_{-0.08}$
52	00:45:49.616	00:45:50.493	00:45:49.738	0.513	$1.5^{+0.1}_{-0.1}$	87^{+25}_{-20}	$-8.31^{+0.05}_{-0.05}$
53	00:45:51.468	00:45:51.829	00:45:51.765	0.289	$1.1^{+0.2}_{-0.1}$	124^{+89}_{-53}	$-8.69^{+0.07}_{-0.07}$
54	00:45:55.816	00:45:57.065	00:45:56.514	0.962	$2.2^{+0.4}_{-0.3}$	13^{+5}_{-4}	$-8.57^{+0.06}_{-0.06}$
55	00:45:57.325	00:45:57.553	00:45:57.347	0.088	$2.9^{+0.8}_{-0.5}$	70^{+34}_{-25}	$-7.49^{+0.07}_{-0.07}$
56	00:45:58.054	00:45:59.256	00:45:58.064	0.544	$1.4^{+0.2}_{-0.2}$	59^{+26}_{-19}	$-8.6^{+0.07}_{-0.06}$
57	00:45:59.998	00:46:01.784	00:46:00.687	1.158	$2.71^{+0.06}_{-0.06}$	400^{+18}_{-17}	$-6.81^{+0.01}_{-0.01}$

Table 2
(Continued)

Burst No.	$T_{\text{st},100}$ (UTC)	$T_{\text{et},100}$ (UTC)	T_{peak} (UTC)	T_{90} (s)	kT (keV)	R^2 (km ²)	$\log_{10} F$ (erg cm ⁻² s ⁻¹)
58	00:46:03.706	00:46:07.398	00:46:06.445	2.511	$2.05^{+0.07}_{-0.06}$	84^{+7}_{-6}	$-7.84^{+0.01}_{-0.01}$
59	00:46:07.737	00:46:08.438	00:46:08.257	0.602	$1.3^{+0.3}_{-0.2}$	37^{+24}_{-15}	$-8.83^{+0.09}_{-0.08}$
60	00:46:11.078	00:46:12.430	00:46:12.379	1.277	$1.1^{+0.1}_{-0.1}$	42^{+18}_{-13}	$-9.1^{+0.06}_{-0.06}$
61	00:46:14.090	00:46:15.122	00:46:14.233	0.84	$1.4^{+0.1}_{-0.1}$	53^{+17}_{-13}	$-8.62^{+0.05}_{-0.05}$
62	00:46:15.566	00:46:19.285	00:46:18.015	2.852	$1.97^{+0.05}_{-0.05}$	120^{+8}_{-7}	$-7.74^{+0.01}_{-0.01}$
63	00:46:19.974	00:46:25.147	00:46:20.243	4.519	$2.77^{+0.04}_{-0.04}$	270^{+7}_{-7}	$-6.95^{+0.01}_{-0.01}$
64	00:46:26.731	00:46:28.005	00:46:27.415	1.129	$1.3^{+0.2}_{-0.1}$	68^{+31}_{-21}	$-8.6^{+0.04}_{-0.04}$
65	00:46:28.483	00:46:31.186	00:46:29.769	1.263	$2.1^{+0.1}_{-0.1}$	80^{+10}_{-9}	$-7.86^{+0.02}_{-0.02}$
66	00:46:33.057	00:46:38.340	00:46:33.658	3.7	$1.97^{+0.05}_{-0.05}$	86^{+6}_{-6}	$-7.88^{+0.01}_{-0.01}$
67	00:46:38.741	00:46:41.797	00:46:40.541	1.906	$1.59^{+0.09}_{-0.08}$	55^{+9}_{-8}	$-8.38^{+0.03}_{-0.03}$
68	00:46:42.755	00:46:44.073	00:46:43.237	0.61	$2.98^{+0.09}_{-0.08}$	430^{+25}_{-24}	$-6.67^{+0.01}_{-0.01}$
69	00:46:45.733	00:46:48.221	00:46:46.829	1.45	$1.23^{+0.09}_{-0.08}$	70^{+16}_{-14}	$-8.69^{+0.04}_{-0.04}$
70	00:46:48.223	00:46:49.132	00:46:48.887	0.697	$2.0^{+0.4}_{-0.3}$	19^{+6}_{-6}	$-8.54^{+0.07}_{-0.07}$
71	00:46:50.226	00:46:51.328	00:46:50.557	0.923	$1.6^{+0.1}_{-0.1}$	54^{+12}_{-10}	$-8.35^{+0.04}_{-0.04}$
72	00:46:54.959	00:46:57.714	00:46:56.705	2.204	$1.76^{+0.07}_{-0.06}$	82^{+8}_{-8}	$-8.06^{+0.02}_{-0.02}$
73	00:46:58.863	00:47:00.752	00:46:59.743	0.904	$1.66^{+0.07}_{-0.06}$	180^{+20}_{-18}	$-7.81^{+0.02}_{-0.02}$
74	00:47:01.372	00:47:02.979	00:47:02.017	1.086	$1.9^{+0.2}_{-0.1}$	38^{+8}_{-7}	$-8.32^{+0.04}_{-0.04}$
75	00:47:03.530	00:47:06.365	00:47:04.505	1.721	$2.0^{+0.1}_{-0.1}$	66^{+8}_{-7}	$-7.98^{+0.02}_{-0.02}$
76	00:47:08.250	00:47:11.064	00:47:09.756	2.044	$1.3^{+0.1}_{-0.1}$	45^{+11}_{-9}	$-8.76^{+0.04}_{-0.04}$
77	00:47:11.560	00:47:16.812	00:47:14.611	4.472	$1.76^{+0.06}_{-0.06}$	50^{+5}_{-4}	$-8.28^{+0.02}_{-0.02}$
78	00:47:18.051	00:47:19.906	00:47:18.948	0.91	$2.01^{+0.07}_{-0.07}$	194^{+17}_{-16}	$-7.5^{+0.02}_{-0.02}$
79	00:47:24.515	00:47:25.576	00:47:25.105	0.711	$2.4^{+0.1}_{-0.1}$	210^{+18}_{-17}	$-7.27^{+0.02}_{-0.02}$
80	00:47:26.949	00:47:27.578	00:47:27.151	0.409	$1.4^{+0.3}_{-0.2}$	48^{+25}_{-17}	$-8.6^{+0.08}_{-0.07}$
81	00:47:30.365	00:47:31.241	00:47:30.390	0.789	$1.1^{+0.2}_{-0.1}$	56^{+30}_{-20}	$-8.98^{+0.07}_{-0.07}$
82	00:47:31.729	00:47:32.925	00:47:32.145	0.579	$2.0^{+0.1}_{-0.1}$	130^{+19}_{-17}	$-7.72^{+0.03}_{-0.03}$
83	00:47:34.858	00:47:36.364	00:47:35.689	0.809	$2.17^{+0.07}_{-0.06}$	300^{+22}_{-20}	$-7.21^{+0.01}_{-0.01}$
84	00:47:38.281	00:47:39.484	00:47:39.312	0.861	$1.3^{+0.1}_{-0.1}$	71^{+21}_{-17}	$-8.58^{+0.05}_{-0.05}$
85	00:47:41.916	00:47:42.307	00:47:41.968	0.324	$1.5^{+0.3}_{-0.2}$	80^{+37}_{-27}	$-8.35^{+0.08}_{-0.07}$
86	00:47:43.310	00:47:43.516	00:47:43.459	0.157
87	00:47:44.125	00:47:46.512	00:47:44.331	1.941	$1.7^{+0.1}_{-0.1}$	35^{+7}_{-6}	$-8.49^{+0.03}_{-0.03}$
88	00:47:46.827	00:47:47.843	00:47:47.056	0.826	$1.8^{+0.4}_{-0.3}$	15^{+8}_{-6}	$-8.81^{+0.08}_{-0.08}$
89	00:47:51.486	00:47:52.608	00:47:52.328	0.719	$2.02^{+0.08}_{-0.08}$	200^{+20}_{-19}	$-7.48^{+0.02}_{-0.02}$
90	00:47:56.487	00:47:56.836	00:47:56.536	0.136	$1.9^{+1.0}_{-0.5}$	25^{+28}_{-15}	$-8.5^{+0.2}_{-0.1}$
91	00:47:57.478	00:47:58.779	00:47:57.573	0.748	$2.45^{+0.08}_{-0.07}$	300^{+21}_{-19}	$-7.06^{+0.01}_{-0.01}$
92	00:47:59.713	00:48:02.092	00:48:00.243	1.446	$1.9^{+0.06}_{-0.06}$	170^{+14}_{-13}	$-7.63^{+0.01}_{-0.01}$
93	00:48:07.963	00:48:08.779	00:48:08.251	0.453	$2.1^{+0.2}_{-0.2}$	85^{+18}_{-15}	$-7.82^{+0.04}_{-0.03}$
94	00:48:20.336	00:48:24.484	00:48:23.754	3.508	$1.5^{+0.1}_{-0.1}$	26^{+5}_{-4}	$-8.76^{+0.03}_{-0.03}$
95	00:48:26.817	00:48:28.266	00:48:27.020	1.129	$1.79^{+0.07}_{-0.07}$	140^{+15}_{-14}	$-7.81^{+0.02}_{-0.02}$
96	00:48:32.660	00:48:34.477	00:48:33.367	0.938	$1.98^{+0.08}_{-0.08}$	150^{+15}_{-14}	$-7.63^{+0.02}_{-0.02}$
97	00:48:43.468	00:48:46.029	00:48:44.858	0.644	$2.55^{+0.07}_{-0.07}$	430^{+26}_{-25}	$-6.85^{+0.01}_{-0.01}$
98	00:48:48.288	00:48:52.294	00:48:49.317	2.339	$2.68^{+0.06}_{-0.05}$	210^{+9}_{-9}	$-7.1^{+0.01}_{-0.01}$
99	00:48:52.729	00:48:57.134	00:48:56.199	3.788	$1.89^{+0.05}_{-0.05}$	88^{+6}_{-6}	$-7.93^{+0.01}_{-0.01}$
100	00:48:57.369	00:49:28.181	00:48:57.373	30.811	$2.15^{+0.02}_{-0.02}$	180^{+5}_{-5}	$-7.43^{+0.01}_{-0.01}$
101	00:49:32.031	00:49:33.119	00:49:32.702	0.821	$1.27^{+0.09}_{-0.08}$	130^{+28}_{-24}	$-8.35^{+0.04}_{-0.03}$
102	00:49:33.351	00:49:34.533	00:49:34.115	0.853	$2.1^{+0.2}_{-0.2}$	42^{+9}_{-7}	$-8.1^{+0.03}_{-0.03}$
103	00:49:35.236	00:49:36.404	00:49:35.948	0.799	$1.99^{+0.07}_{-0.07}$	220^{+20}_{-19}	$-7.47^{+0.02}_{-0.02}$
104	00:49:36.805	00:49:38.391	00:49:36.957	1.281	$1.4^{+0.1}_{-0.1}$	35^{+11}_{-9}	$-8.77^{+0.05}_{-0.05}$
105	00:49:38.688	00:49:41.148	00:49:40.293	2.106	$1.6^{+0.1}_{-0.1}$	39^{+7}_{-6}	$-8.49^{+0.03}_{-0.03}$
106	00:49:41.984	00:49:43.944	00:49:42.741	1.408	$1.58^{+0.09}_{-0.08}$	72^{+12}_{-10}	$-8.28^{+0.03}_{-0.03}$
107	00:49:45.692	00:49:49.384	00:49:46.772	1.321	$2.72^{+0.07}_{-0.07}$	220^{+13}_{-12}	$-7.06^{+0.01}_{-0.01}$
108	00:49:49.575	00:49:50.140	00:49:50.079	0.484	$1.5^{+0.2}_{-0.2}$	50^{+21}_{-15}	$-8.57^{+0.07}_{-0.06}$
109	00:49:50.658	00:49:53.730	00:49:52.271	2.119	$1.92^{+0.09}_{-0.08}$	59^{+7}_{-6}	$-8.08^{+0.02}_{-0.02}$
110	00:49:54.529	00:49:56.177	00:49:55.078	1.197	$1.41^{+0.08}_{-0.08}$	89^{+16}_{-14}	$-8.36^{+0.03}_{-0.03}$
111	00:49:56.997	00:50:02.615	00:50:01.371	3.538	$2.49^{+0.05}_{-0.05}$	140^{+6}_{-6}	$-7.36^{+0.01}_{-0.01}$
112	00:50:03.039	00:50:04.943	00:50:03.786	0.803	$2.1^{+0.1}_{-0.1}$	87^{+13}_{-11}	$-7.83^{+0.03}_{-0.03}$
113	00:50:05.322	00:50:05.908	00:50:05.664	0.44	$1.28^{+0.09}_{-0.08}$	210^{+47}_{-39}	$-8.14^{+0.04}_{-0.03}$
114	00:50:09.077	00:50:09.690	00:50:09.487	0.424	$1.8^{+0.3}_{-0.2}$	35^{+15}_{-11}	$-8.37^{+0.07}_{-0.07}$

Table 2
(Continued)

Burst No.	$T_{\text{et},100}$ (UTC)	$T_{\text{et},100}$ (UTC)	T_{peak} (UTC)	T_{90} (s)	kT (keV)	R^2 (km ²)	$\log_{10} F$ (erg cm ⁻² s ⁻¹)
115	00:50:11.166	00:50:11.870	00:50:11.182	0.624	$1.2^{+0.2}_{-0.1}$	65^{+30}_{-21}	$-8.77^{+0.07}_{-0.06}$
116	00:50:13.445	00:50:15.528	00:50:14.097	1.952	$1.5^{+0.1}_{-0.1}$	43^{+8}_{-7}	$-8.54^{+0.03}_{-0.03}$
117	00:50:16.502	00:50:17.943	00:50:17.529	1.172	$1.56^{+0.09}_{-0.08}$	85^{+14}_{-12}	$-8.23^{+0.03}_{-0.03}$
118	00:50:19.672	00:50:22.559	00:50:22.013	2.242	$2.04^{+0.06}_{-0.06}$	120^{+9}_{-8}	$-7.71^{+0.01}_{-0.01}$
119	00:50:30.649	00:50:30.973	00:50:30.726	0.237	$1.2^{+0.5}_{-0.3}$	61^{+71}_{-36}	$-8.8^{+0.2}_{-0.1}$
120	00:50:34.424	00:50:35.720	00:50:34.936	0.674	$1.9^{+0.1}_{-0.1}$	150^{+19}_{-18}	$-7.71^{+0.02}_{-0.02}$
121	00:50:39.025	00:50:41.308	00:50:39.645	1.926	$1.9^{+0.1}_{-0.1}$	54^{+7}_{-6}	$-8.14^{+0.02}_{-0.02}$
122	00:50:41.808	00:50:43.410	00:50:41.854	0.589	$2.2^{+0.1}_{-0.1}$	180^{+19}_{-18}	$-7.41^{+0.02}_{-0.02}$
123	00:50:44.090	00:50:45.374	00:50:45.171	1.159	$1.4^{+0.2}_{-0.1}$	35^{+13}_{-10}	$-8.83^{+0.06}_{-0.05}$
124	00:50:49.604	00:50:49.837	00:50:49.691	0.191	$1.1^{+0.2}_{-0.1}$	180^{+100}_{-67}	$-8.54^{+0.07}_{-0.07}$
125	00:50:50.202	00:50:51.121	00:50:50.751	0.748	$1.4^{+0.2}_{-0.1}$	42^{+16}_{-12}	$-8.73^{+0.06}_{-0.06}$
126	00:50:53.950	00:50:55.966	00:50:54.793	1.273	$1.6^{+0.2}_{-0.1}$	6^{+9}_{-7}	$-8.55^{+0.04}_{-0.04}$
127	00:50:58.262	00:50:58.915	00:50:58.869	0.605	$1.3^{+0.4}_{-0.2}$	25^{+23}_{-13}	$-9.11^{+0.1}_{-0.1}$
128	00:50:59.373	00:51:00.209	00:51:00.078	0.669	$1.0^{+0.3}_{-0.2}$	46^{+51}_{-26}	$-9.3^{+0.1}_{-0.1}$
129	00:51:00.731	00:51:01.874	00:51:01.562	0.975	$1.4^{+0.3}_{-0.2}$	22^{+13}_{-9}	$-8.96^{+0.09}_{-0.08}$
130	00:51:03.472	00:51:05.917	00:51:04.668	0.747	$1.99^{+0.06}_{-0.06}$	300^{+24}_{-22}	$-7.32^{+0.01}_{-0.01}$
131	00:51:07.203	00:51:07.937	00:51:07.723	0.674	$1.1^{+0.2}_{-0.1}$	47^{+31}_{-19}	$-9.11^{+0.08}_{-0.08}$
132	00:51:10.880	00:51:11.067	00:51:10.887	0.143	$0.9^{+0.2}_{-0.1}$	270^{+214}_{-123}	$-8.64^{+0.08}_{-0.08}$
133	00:51:12.408	00:51:13.300	00:51:12.758	0.421	$0.8^{+0.2}_{-0.1}$	130^{+110}_{-1}	$-9.06^{+0.08}_{-0.08}$
134	00:51:14.367	00:51:15.220	00:51:15.032	0.786	$1.5^{+0.2}_{-0.2}$	25^{+11}_{-8}	$-8.81^{+0.07}_{-0.07}$
135	00:51:15.791	00:51:16.934	00:51:16.746	0.942	$1.6^{+0.3}_{-0.2}$	17^{+8}_{-6}	$-8.86^{+0.07}_{-0.07}$
136	00:51:19.196	00:51:20.702	00:51:19.399	1.083	$1.65^{+0.06}_{-0.06}$	170^{+18}_{-17}	$-7.83^{+0.02}_{-0.02}$
137	00:51:22.604	00:51:24.764	00:51:23.832	1.493	$2.0^{+0.2}_{-0.2}$	19^{+5}_{-4}	$-8.51^{+0.04}_{-0.04}$
138	00:51:25.767	00:51:27.434	00:51:26.980	1.29	$1.37^{+0.08}_{-0.07}$	98^{+16}_{-14}	$-8.37^{+0.03}_{-0.03}$
139	00:51:30.529	00:51:33.113	00:51:32.226	1.532	$1.49^{+0.09}_{-0.08}$	73^{+12}_{-11}	$-8.37^{+0.03}_{-0.03}$
140	00:51:35.325	00:51:36.754	00:51:35.932	0.525	$2.43^{+0.09}_{-0.08}$	340^{+26}_{-25}	$-7.02^{+0.01}_{-0.01}$
141	00:51:54.916	00:51:56.684	00:51:55.467	0.757	$2.41^{+0.07}_{-0.07}$	330^{+22}_{-21}	$-7.04^{+0.01}_{-0.01}$
142	00:52:05.906	00:52:08.335	00:52:06.245	0.636	$2.3^{+0.1}_{-0.1}$	130^{+16}_{-14}	$-7.47^{+0.02}_{-0.02}$
143	00:52:09.678	00:52:10.788	00:52:10.355	0.875	$1.2^{+0.2}_{-0.1}$	41^{+18}_{-13}	$-8.93^{+0.06}_{-0.06}$
144	00:52:16.571	00:52:17.667	00:52:16.596	1.032	$1.0^{+0.2}_{-0.2}$	30^{+25}_{-14}	$-9.4^{+0.1}_{-0.1}$
145	00:52:18.925	00:52:20.712	00:52:19.884	1.352	$1.67^{+0.09}_{-0.08}$	70^{+11}_{-9}	$-8.21^{+0.03}_{-0.03}$
146	00:52:25.260	00:52:25.969	00:52:25.320	0.655	$1.1^{+0.2}_{-0.1}$	57^{+34}_{-22}	$-9.02^{+0.08}_{-0.08}$
147	00:52:28.128	00:52:28.881	00:52:28.554	0.565	$1.5^{+0.5}_{-0.3}$	23^{+21}_{-12}	$-8.9^{+0.1}_{-0.1}$
148	00:52:34.103	00:52:35.064	00:52:34.931	0.792	$1.8^{+0.3}_{-0.2}$	25^{+10}_{-7}	$-8.58^{+0.06}_{-0.06}$
149	00:52:36.287	00:52:37.256	00:52:36.998	0.885	$2.2^{+0.5}_{-0.3}$	9^{+5}_{-3}	$-8.7^{+0.07}_{-0.07}$
150	00:52:37.706	00:52:38.508	00:52:37.807	0.555	$1.3^{+0.1}_{-0.1}$	95^{+32}_{-25}	$-8.5^{+0.06}_{-0.05}$
151	00:52:39.462	00:52:40.935	00:52:40.158	0.811	$1.0^{+0.1}_{-0.1}$	90^{+32}_{-24}	$-8.85^{+0.05}_{-0.05}$
152	00:52:44.491	00:52:45.536	00:52:44.761	0.899	$1.4^{+0.2}_{-0.2}$	32^{+13}_{-9}	$-8.81^{+0.06}_{-0.06}$
153	00:52:48.433	00:52:49.067	00:52:48.753	0.513	$1.6^{+0.3}_{-0.2}$	36^{+16}_{-12}	$-8.53^{+0.07}_{-0.07}$
154	00:52:49.637	00:52:50.103	00:52:49.700	0.412	$2.2^{+0.8}_{-0.4}$	14^{+10}_{-7}	$-8.5^{+0.1}_{-0.1}$
155	00:52:53.507	00:52:54.099	00:52:53.591	0.549	$1.3^{+0.3}_{-0.2}$	24^{+19}_{-11}	$-9.1^{+0.1}_{-0.1}$
156	00:52:54.982	00:52:56.013	00:52:55.223	0.629	$3.0^{+0.4}_{-0.3}$	28^{+7}_{-6}	$-7.87^{+0.04}_{-0.04}$
157	00:53:09.712	00:53:10.469	00:53:09.842	0.505	$1.4^{+0.1}_{-0.1}$	110^{+28}_{-23}	$-8.28^{+0.04}_{-0.04}$
158	00:53:24.194	00:53:26.949	00:53:25.144	1.667	$1.52^{+0.04}_{-0.04}$	220^{+18}_{-17}	$-7.85^{+0.01}_{-0.01}$
159	00:53:28.982	00:53:29.949	00:53:29.106	0.896	$1.5^{+0.3}_{-0.2}$	17^{+9}_{-6}	$-8.93^{+0.08}_{-0.08}$
160	00:53:30.310	00:53:30.390	00:53:30.342	0.064
161	00:53:37.836	00:53:40.169	00:53:38.865	1.438	$2.03^{+0.06}_{-0.06}$	180^{+13}_{-13}	$-7.51^{+0.01}_{-0.01}$
162	00:53:41.691	00:53:42.150	00:53:41.866	0.23	$2.0^{+0.6}_{-0.4}$	28^{+18}_{-12}	$-8.4^{+0.1}_{-0.1}$
163	00:53:45.002	00:53:45.823	00:53:45.267	0.582	$1.4^{+0.2}_{-0.2}$	45^{+19}_{-14}	$-8.63^{+0.07}_{-0.06}$
164	00:53:48.619	00:53:49.493	00:53:48.630	0.655	$1.0^{+0.2}_{-0.1}$	52^{+35}_{-22}	$-9.11^{+0.08}_{-0.08}$
165	00:53:51.979	00:53:54.304	00:53:52.330	0.518	$2.1^{+0.1}_{-0.1}$	210^{+23}_{-21}	$-7.42^{+0.02}_{-0.02}$
166	00:53:58.858	00:53:59.338	00:53:59.009	0.258	$1.0^{+0.2}_{-0.1}$	130^{+76}_{-49}	$-8.71^{+0.08}_{-0.08}$
167	00:54:03.982	00:54:04.455	00:54:04.045	0.309	$1.5^{+0.4}_{-0.3}$	37^{+27}_{-17}	$-8.7^{+0.1}_{-0.1}$
168	00:54:06.986	00:54:08.459	00:54:07.803	1.124	$1.3^{+0.3}_{-0.2}$	14^{+11}_{-7}	$-9.3^{+0.1}_{-0.1}$
169	00:54:10.816	00:54:11.717	00:54:10.899	0.524	$2.1^{+0.3}_{-0.2}$	43^{+12}_{-10}	$-8.10^{+0.05}_{-0.04}$
170	00:54:12.364	00:54:14.865	00:54:13.657	2.053	$1.4^{+0.1}_{-0.1}$	22^{+7}_{-5}	$-9.00^{+0.05}_{-0.05}$
171	00:54:27.094	00:54:28.184	00:54:27.206	0.291	$2.4^{+0.3}_{-0.2}$	76^{+18}_{-15}	$-7.70^{+0.04}_{-0.04}$

Table 2
(Continued)

Burst No.	$T_{st,100}$ (UTC)	$T_{et,100}$ (UTC)	T_{peak} (UTC)	T_{90} (s)	kT (keV)	R^2 (km ²)	$\log_{10} F$ (erg cm ⁻² s ⁻¹)
172	00:54:28.759	00:54:29.723	00:54:29.083	0.596	1.4 ^{+0.1} _{-0.1}	75 ⁺²² ₋₁₈	-8.46 ^{+0.05} _{-0.05}
173	00:54:31.305	00:54:31.503	00:54:31.380	0.132
174	00:54:45.094	00:54:45.445	00:54:45.166	0.239	1.4 ^{+0.5} _{-0.3}	52 ⁺⁵² ₋₂₈	-8.6 ^{+0.1} _{-0.1}
175	00:54:45.893	00:54:47.504	00:54:46.135	1.076	1.9 ^{+0.2} _{-0.1}	34 ⁺⁸ ₋₇	-8.36 ^{+0.04} _{-0.04}
176	00:54:48.694	00:54:50.134	00:54:49.606	1.212	1.9 ^{+0.3} _{-0.2}	13 ⁺⁵ ₋₄	-8.72 ^{+0.06} _{-0.06}
177	00:54:52.418	00:54:54.214	00:54:53.356	1.549	2.4 ⁺² _{-0.7}	3 ⁺³ ₋₂	-9.1 ^{+0.2} _{-0.1}
178	00:54:56.294	00:55:00.410	00:54:57.506	1.75	2.9 ^{+0.1} _{-0.1}	160 ⁺⁹ ₋₈	-7.15 ^{+0.01} _{-0.01}
179	00:55:04.966	00:55:05.956	00:55:05.902	0.947	2.6 ⁺² _{-0.7}	3 ⁺³ ₋₂	-9.0 ^{+0.1} _{-0.1}
180	00:55:07.227	00:55:08.359	00:55:07.428	0.995	1.5 ^{+0.2} _{-0.2}	30 ⁺¹² ₋₉	-8.71 ^{+0.07} _{-0.06}
181	00:55:15.923	00:55:16.818	00:55:16.313	0.696	1.1 ^{+0.2} _{-0.2}	43 ⁺³⁰ ₋₁₈	-9.11 ^{+0.09} _{-0.08}
182	00:55:21.964	00:55:23.251	00:55:22.728	0.703	1.7 ^{+0.2} _{-0.1}	65 ⁺¹⁵ ₋₁₃	-8.21 ^{+0.04} _{-0.04}
183	00:55:32.652	00:55:33.519	00:55:33.087	0.656	1.5 ^{+0.3} _{-0.2}	20 ⁺¹¹ ₋₈	-8.89 ^{+0.09} _{-0.08}
184	00:55:36.705	00:55:37.475	00:55:37.363	0.546
185	00:55:39.902	00:55:40.236	00:55:39.985	0.222	1.9 ^{+0.3} _{-0.2}	64 ⁺²⁶ ₋₁₉	-8.04 ^{+0.06} _{-0.06}
186	00:55:42.231	00:55:43.249	00:55:42.913	0.91	1.4 ^{+0.2} _{-0.2}	31 ⁺¹³ ₋₉	-8.8 ^{+0.06} _{-0.06}
187	00:55:54.569	00:55:58.916	00:55:56.351	2.408	1.9 ^{+0.1} _{-0.1}	51 ⁺⁶ ₋₅	-8.16 ^{+0.02} _{-0.02}
188	00:56:03.231	00:56:05.963	00:56:04.480	2.209	1.0 ^{+0.1} _{-0.1}	33 ⁺¹⁵ ₋₁₀	-9.36 ^{+0.06} _{-0.06}
189	00:56:14.911	00:56:17.318	00:56:16.715	1.829	2.4 ^{+0.4} _{-0.3}	8 ⁺³ ₋₂	-8.67 ^{+0.05} _{-0.05}
190	00:56:18.852	00:56:22.785	00:56:20.144	2.813	1.7 ^{+0.1} _{-0.1}	30 ⁺⁵ ₋₄	-8.59 ^{+0.03} _{-0.03}
191	00:56:24.810	00:56:25.919	00:56:24.827	0.808	1.4 ^{+0.1} _{-0.1}	95 ⁺²¹ ₋₁₇	-8.37 ^{+0.04} _{-0.04}
192	00:56:27.624	00:56:27.778	00:56:27.635	0.139
193	00:56:36.565	00:56:37.742	00:56:36.597	1.082	1.6 ^{+0.5} _{-0.3}	10 ⁺⁷ ₋₅	-9.1 ^{+0.1} _{-0.1}
194	00:56:42.355	00:56:44.586	00:56:42.937	1.133	2.3 ⁺¹ _{-0.6}	4 ⁺³ ₋₂	-9.1 ^{+0.1} _{-0.1}
195	00:56:45.939	00:56:46.110	00:56:46.009	0.085	1.2 ^{+0.5} _{-0.3}	130 ⁺¹⁵⁰ ₋₇₄	-8.5 ^{+0.2} _{-0.1}
196	00:56:48.694	00:56:51.315	00:56:49.842	0.712	2.27 ^{+0.07} _{-0.06}	380 ⁺²⁵ ₋₂₄	-7.05 ^{+0.01} _{-0.01}
197	00:57:00.538	00:57:01.365	00:57:00.921	0.604	2.0 ^{+0.6} _{-0.4}	14 ⁺⁸ ₋₆	-8.7 ^{+0.1} _{-0.1}
198	00:57:05.060	00:57:05.354	00:57:05.089	0.084
199	00:57:20.313	00:57:20.770	00:57:20.368	0.293	2.2 ^{+0.4} _{-0.3}	33 ⁺¹⁴ ₋₁₁	-8.17 ^{+0.07} _{-0.06}
200	00:57:22.727	00:57:23.894	00:57:23.647	0.823	1.8 ^{+0.3} _{-0.2}	15 ⁺⁷ ₋₅	-8.74 ^{+0.07} _{-0.07}
201	00:57:28.352	00:57:29.815	00:57:28.429	1.228	1.3 ^{+0.6} _{-0.3}	8.6 ⁺¹¹ ₋₅	-9.6 ^{+0.2} _{-0.2}
202	00:57:35.366	00:57:36.718	00:57:35.854	1.059	1.4 ^{+0.1} _{-0.1}	53 ⁺¹³ ₋₁₁	-8.56 ^{+0.04} _{-0.04}
203	00:57:45.709	00:57:46.407	00:57:46.063	0.54	1.6 ^{+0.4} _{-0.3}	24 ⁺¹⁵ ₋₁₀	-8.7 ^{+0.1} _{-0.1}
204	00:57:48.155	00:57:48.759	00:57:48.299	0.091	2.9 ^{+0.6} _{-0.4}	100 ⁺³⁶ ₋₂₉	-7.32 ^{+0.05} _{-0.05}
205	00:57:53.779	00:57:54.492	00:57:54.070	0.578	1.5 ^{+0.3} _{-0.3}	29 ⁺¹⁵ ₋₁₀	-8.81 ^{+0.08} _{-0.08}
206	00:57:56.452	00:57:58.414	00:57:57.069	0.878	1.7 ^{+0.1} _{-0.1}	91 ⁺¹⁵ ₋₁₃	-8.06 ^{+0.03} _{-0.03}
207	00:58:02.249	00:58:03.098	00:58:03.009	0.499
208	00:58:05.090	00:58:05.783	00:58:05.625	0.508	1.4 ^{+0.6} _{-0.3}	11.15 ⁺¹⁴ ₋₇	-9.3 ^{+0.2} _{-0.1}
209	00:58:12.219	00:58:12.485	00:58:12.225	0.228	1.9 ⁺¹ _{-0.5}	12.42 ⁺¹⁷ ₋₈	-8.8 ^{+0.2} _{-0.2}
210	00:58:18.286	00:58:18.534	00:58:18.326	0.211	1.9 ^{+0.5} _{-0.3}	38 ⁺²² ₋₁₅	-8.27 ^{+0.09} _{-0.08}
211	00:58:30.109	00:58:31.671	00:58:31.214	1.429	0.9 ^{+0.2} _{-0.1}	36 ⁺²⁸ ₋₁₆	-9.51 ^{+0.08} _{-0.08}
212	00:58:42.989	00:58:46.172	00:58:45.280	2.232	1.3 ^{+0.04} _{-0.04}	200 ⁺¹⁹ ₋₁₈	-8.20 ^{+0.02} _{-0.02}
213	00:58:47.121	00:58:47.949	00:58:47.429	0.591	1.4 ^{+0.8} _{-0.4}	9 ⁺¹³ ₋₆	-9.3 ^{+0.2} _{-0.2}
214	00:58:50.421	00:58:51.319	00:58:50.622	0.748	1.0 ^{+0.2} _{-0.2}	37 ⁺³⁰ ₋₁₇	-9.3 ^{+0.1} _{-0.1}
215	00:58:52.656	00:58:52.921	00:58:52.678	0.133	1.6 ^{+0.2} _{-0.2}	220 ⁺⁶⁹ ₋₅₄	-7.78 ^{+0.05} _{-0.05}
216	00:58:53.605	00:58:54.700	00:58:53.978	0.547	1.3 ^{+0.2} _{-0.2}	55 ⁺²⁵ ₋₁₈	-8.66 ^{+0.07} _{-0.07}
217	00:58:56.906	00:58:58.271	00:58:57.484	0.825	1.9 ^{+0.1} _{-0.1}	160 ⁺¹⁸ ₋₁₆	-7.68 ^{+0.02} _{-0.02}
218	03:55:37.447	03:55:39.450	03:55:37.683	1.532	0.75 ^{+0.09} _{-0.08}	83 ⁺⁴⁴ ₋₂₉	-9.45 ^{+0.06} _{-0.06}
219	03:56:21.396	03:56:21.828	03:56:21.540	0.383	1.2 ^{+0.3} _{-0.2}	32 ⁺³⁰ ₋₁₇	-9.1 ^{+0.1} _{-0.1}
220	05:26:40.266	05:26:41.375	05:26:40.345	1.029	2.3 ⁺² _{-0.6}	2 ⁺³ ₋₁	-9.4 ^{+0.2} _{-0.2}
221	05:27:55.174	05:27:55.914	05:27:55.325	0.527
222	06:51:54.178	06:51:54.370	06:51:54.208	0.165	0.5 ^{+0.1} _{-0.1}	970 ⁺¹³⁰⁰ ₋₅₆₀	-9.0 ^{+0.1} _{-0.1}
223	07:00:16.717	07:00:16.941	07:00:16.773	0.168	1.7 ^{+0.3} _{-0.2}	53 ⁺²⁶ ₋₁₉	-8.4 ^{+0.1} _{-0.1}

Note. Times of bursts are from 2020 April 28. Fluxes are in the 0.5–10 keV range.

(This table is available in machine-readable form.)

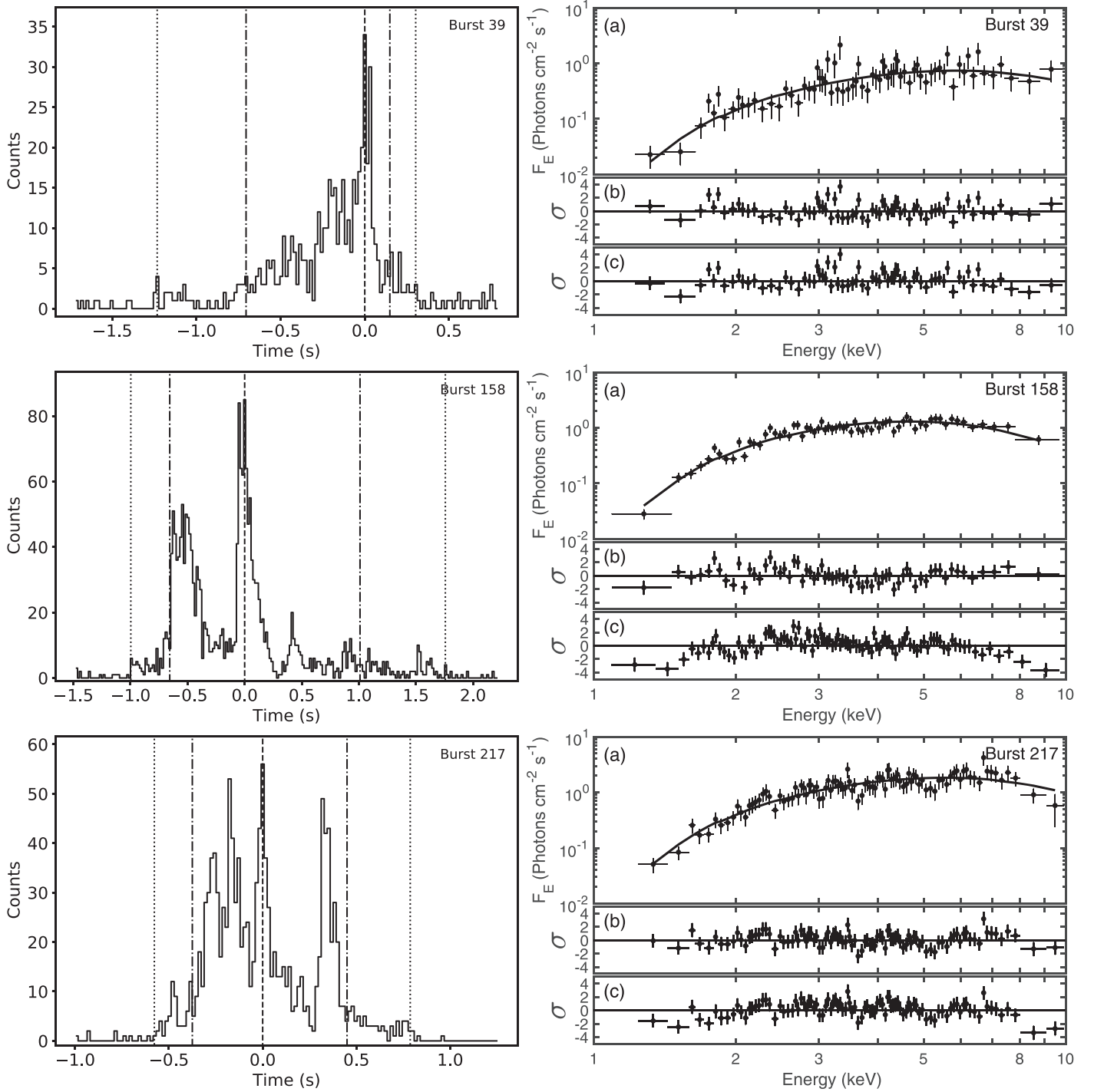


Figure 2. Left panels: three examples of bursts emitted during the burst forest plotted with 16 ms resolution in the 1–10 keV energy range. The vertical dotted lines delimit the T_{100} start and end times of the bursts. The dotted–dashed lines delimit the start and end times of the T_{90} interval. The peak time of the bursts is shown as a dashed line and corresponds to $t = 0$. Right panels: spectra of each of the bursts. Panels (a) show the data in F_E space and the best-fit absorbed BB model. Panels (b) are the corresponding residuals in terms of σ . Panels (c) show the residuals of an absorbed PL model for comparison. See text for details.

interval just before and after these times, respectively. These background intervals range between 0.3 and 2 s. We fit the cumulative count distribution of the background interval with a linear function and then correct the burst cumulative count distribution using this background estimate.

We consider the start (end) time of the burst $T_{s,100}$ ($T_{e,100}$) to be the time at which the cumulative sum rises (drops) to 3σ above (below) the average level of the pre- (post-) burst

background-corrected interval; we calculate the burst fluence as the total number of counts between $T_{s,100}$ and $T_{e,100}$, and we define $T_{100} = T_{e,100} - T_{s,100}$. The T_{90} burst duration is estimated as the time interval during which 5%–95% of the burst fluence is accumulated (Kouveliotou et al. 1993). Figure 2 shows three examples of burst light curves along with their $T_{s,100}$ and $T_{e,100}$ (dotted vertical lines) and the start and end times of the T_{90} interval, $T_{s,90}$ and $T_{e,90}$, respectively

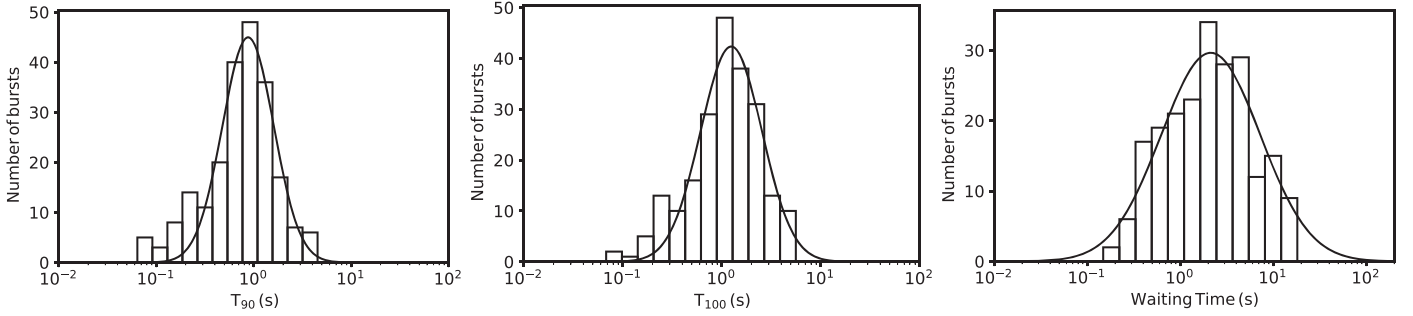


Figure 3. Left panel: T_{90} distribution of the SGR 1935+2154 bursts detected during the burst storm. The black solid line is the best-fit lognormal function to the distribution with a mean of 840 ms. Middle panel: T_{100} distribution along with the best-fit lognormal function (black solid line) with a mean of 1.27 s. Right panel: waiting-time distribution and the best-fit lognormal function, shown as a black solid line. The average waiting time between bursts is 2.1 s. See text for more details.

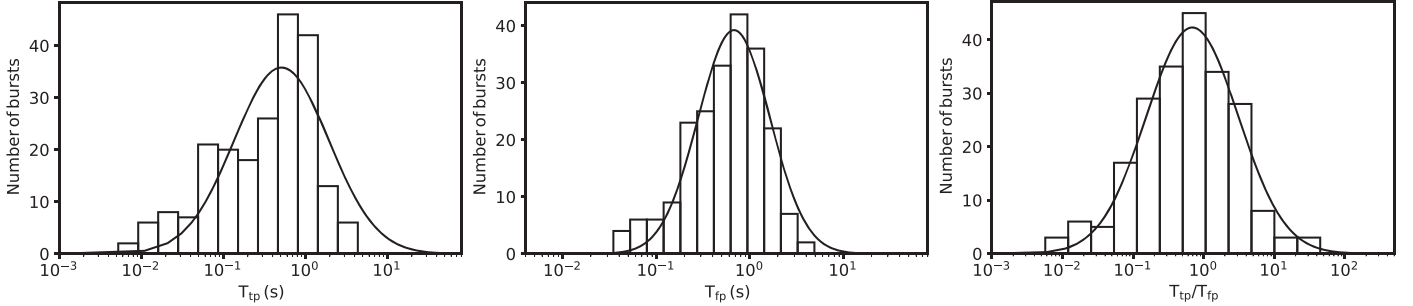


Figure 4. Time to peak (T_{tp} ; left panel), time from peak (T_{fp} ; middle panel), and ratio T_{tp}/T_{fp} (right panel) distributions. The best-fit lognormal function to each distribution is shown as a black solid line with a mean of 510, 680, and 0.69, respectively.

(dotted–dashed vertical lines). The bottom panel of Figure 1 shows the burst storm at 0.5 s resolution after excluding the T_{100} of all bursts.

To establish the peak time of each burst, T_{peak} , we start from the unbinned list of events between $T_{s,100}$ and $T_{e,100}$. We create light curves with a resolution of 2^n ms, where n is an integer iteratively increased from 1 to 6 (i.e., 2–64 ms). Starting with $n = 1$, we define T_{peak} as the first time bin that reaches a total count with significance $>7\sigma$ above the background. If this condition is not met, n is increased and the procedure is repeated until T_{peak} is established. The peak times of the three burst examples are shown as dashed lines in Figure 2. We define the time to peak, T_{tp} , and time from peak, T_{fp} , as $T_{peak} - T_{s,100}$ and $T_{e,100} - T_{peak}$, respectively. Finally, we define the waiting time until the next burst as $T_{i+1,100} - T_{i,100}$, where $i = 1, 2, \dots$, is the burst number.

In the following, we give the statistical properties of the bursts detected during the first GTI, i.e., the burst storm. We later compare their results to the bursts detected in the subsequent four GTIs (Figure 1).

The T_{90} and T_{100} distributions of the bursts are shown in the left and middle panels of Figure 3, respectively. The best-fit lognormal distributions are shown as a black solid line, and the results are in T_{90} and T_{100} means of 840 and 1270 ms. The 1σ interval ranges from 430 to 1630 ms for T_{90} and 620 to 2580 ms for T_{100} . The waiting-time distribution for the bursts identified within the first GTI is shown in the right panel of Figure 3. A fit to the distribution with a lognormal function is shown as a black solid line. We measure a mean of 2.1 s with a 1σ interval range of 0.6–7.2 s. Figure 4 shows the T_{tp} , T_{fp} , and T_{tp}/T_{fp} distributions. The best-fit lognormal distributions to each are shown as black solid lines. We measure a mean time to peak $\langle T_{tp} \rangle = 0.51^{+1.64}_{-0.36}$ s and a mean time from peak $\langle T_{fp} \rangle = 0.68^{+0.96}_{-0.40}$ s. The average of the distribution of the ratio

of these two parameters is $0.69^{+2.40}_{-0.54}$, indicating a steeper rise than decay in the burst profiles. The uncertainties on each parameter represent the 1σ standard deviation of the best-fit lognormal function to the respective distribution.

We searched for any correlation of the burst peak arrival time (after applying a barycentric correction) with rotational phase (Figure 5; light blue dots), given that we detect the source spin period in the four GTIs after the burst storm (see Section 4.1). No clustering is obvious at any particular phase. We find a χ^2 of 15 for 9 dof when fitting the peak arrival data to a horizontal line. We also apply the Anderson–Darling (AD) test to compare the cumulative distribution function of the burst phases to a uniform distribution. We find an AD test statistic of 1.0 and p -value of 0.35, implying that the phases of the bursts are consistent with a uniform distribution. We also tested for the dependence of R^2 , kT , T_{90} , waiting time, and flux on phase and found no significant correlations. Considering very short bursts with $T_{90} < 0.5$ s also results in no significant dependence of any of the burst temporal or spectral parameters with phase. Since the FRB time lands within our observation at a barycentric-corrected time of 58,967.60857593¹⁸ Modified Julian Date (MJD), we also show its arrival time in phase space as a dashed blue line in Figure 5. We discuss the implications of its phase association in Section 5.3.

3.3. Burst Spectral Results

We fit the 1–10 keV spectra of each burst with a simple model consisting of an absorbed blackbody (BB) or PL

¹⁸ We converted the FRB geocentric arrival time to the barycentric reference frame using the tool `pinbary` from the precision timing software `PINT` (Luo et al. 2019; <https://github.com/nanograv/PINT>). We considered the same source position and JPL ephemerides (DE405) as the ones used to barycenter the X-ray data.

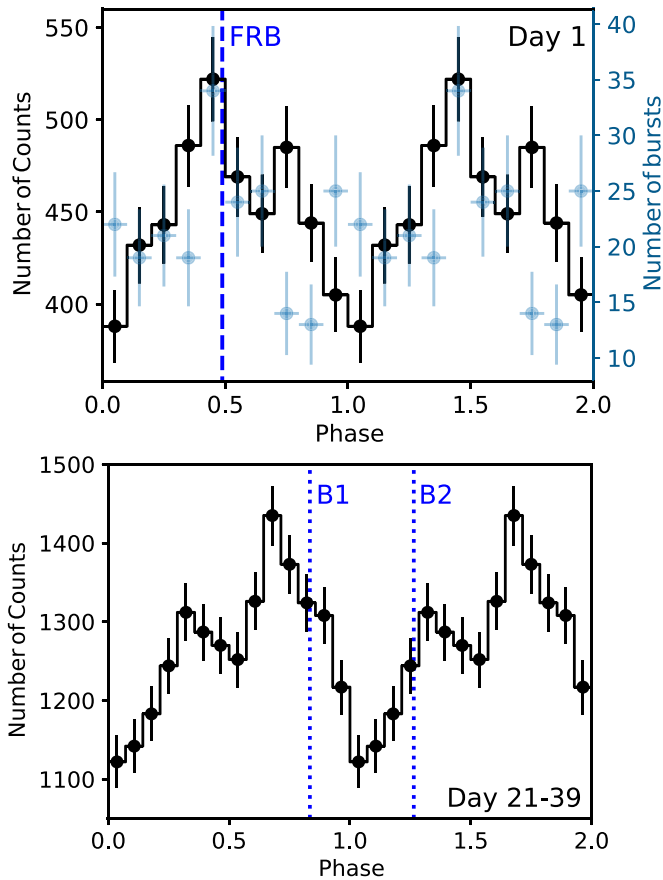


Figure 5. Top panel: persistent emission pulse profile of the NICER data taken on 2020 April 28 (ObsID 3020560101), day 1 after the outburst onset (black dots and solid line). We exclude the first GTI during which the burst forest occurred. The rms pulsed fraction is $8\% \pm 2\%$. The light blue dots represent the peak times of the NICER bursts folded at the spin period of the source. We find no preference for burst peak arrival time with phase. The blue vertical dashed line is the phase of the FRB arrival time. Bottom panel: pulse profile of the persistent emission as observed during days 21–39 postoutburst (ObsIDs 3020560105–3020560119). The dotted lines are the phases of the two radio bursts observed by Kirsten et al. (2020). The rms pulsed fraction is $6.7\% \pm 0.8\%$. The two profiles, shown in the energy range 1.5–5 keV, are not phase-connected; their respective minima are shifted to phase zero. See text for more details.

function. We do not attempt more complex models, such as a cutoff PL or a 2BB model, since NICER only covers a small range of the magnetar burst broadband energy spectrum (~ 1 –200 keV). We could not constrain the hydrogen column density in the direction of SGR 1935+2154 due to the low total number of counts in the majority of the bursts. Hence, we fix N_{H} to $2.4 \times 10^{22} \text{ cm}^{-2}$, which is the best-fit value as derived with high signal-to-noise ratio (S/N) persistent emission spectra of the source (e.g., Younes et al. 2017b). This value is also consistent with the one derived for bursts with enough counts to enable a measurement of N_{H} . Finally, 12 bursts had very few counts to allow for any spectral analysis (Table 2).

We find that most bursts were better fit with the BB model as opposed to the PL one, which consistently resulted in residuals at the lower and upper end of the NICER energy range. We show three examples of burst spectra in the right panels of Figure 2. The spectra and best-fit absorbed BB model are shown in panels (a). The residuals of the absorbed BB and PL are displayed in panels (b) and (c), respectively. As can be seen, especially in the second and third bursts, significant

residuals remain at the lower and upper ends of the energy coverage when the bursts are fit with the PL model.

The distribution of the BB fit temperatures is exhibited in Figure 6 (left panel). We find an average BB temperature of 1.7 and a 1σ range of 1.3–2.2 keV. Assuming a spherically emitting region obeying the Stefan–Boltzmann law $R^2 T^4 = \text{constant}$, we also display the distribution of emission areas R^2 in Figure 6 and estimate an average of 54 km^2 . The 1σ interval is 30–154 km^2 . Both are substantially larger than the corresponding values for the persistent emission as presented in Section 4. Finally, the positive correlation between the BB temperatures, kT , and burst fluxes (Figure 6, right panel) indicates a hardening of burst spectra with increasing flux. However, we should stress the caveat here that we are using a very narrow energy range to derive these results, which might underrepresent the source spectral properties.

We measure burst fluences, F , by multiplying the time-averaged flux of each burst with the corresponding T_{90} (measured in Section 3.2). We show in Figure 7 the differential fluence distribution of the bursts in the first GTI, uniformly binned on a logarithmic scale. The turnover at fluences $\lesssim 1.5 \times 10^{-9}$ (open squares) reflects our inability to recover bursts with lower fluences. To verify this assumption, we perform simple simulations as follows. We assume that a burst is approximated with a top-hat profile of a certain width $w \sim T_{90}$. We assume that the simulated bursts have a total number of counts ranging from 50 to 500, which we iteratively increase in steps of 5 counts. We distribute these counts along w following an exponential distribution, i.e., the expected waiting time between events for a Poisson process. For each total number of counts, we simulate 10^4 bursts with w drawn from the lognormal distribution that best fits the T_{90} distribution. We add a background contribution to the burst in a ± 5 s interval around its centroid. The background count rate is drawn from a normal distribution with a mean and standard deviation of $75 \pm 5 \text{ counts s}^{-1}$, which is the maximum average background count rate of the first GTI (Figure 1, bottom panel). Running our burst search algorithm on the simulated light curves, we find that for 110 total burst counts, we detect the bursts at the 99% rate. For a typical burst spectrum (BB with $kT = 1.7$ keV; see below), this corresponds to a burst fluence $F \sim 1.6 \times 10^{-9} \text{ erg cm}^{-2}$. Ignoring the bins in Figure 7 with fluences lower than this value, we find that the differential fluence distribution for SGR 1935+2154 bursts can be well modeled with a power law (PL) $N \propto F^{-0.5 \pm 0.1}$ or $dN/dF \propto F^{-1.5 \pm 0.1}$, where N represents the total number of bursts within a fluence bin, over approximately 3 orders of magnitude of fluence from 10^{-6} to $10^{-9} \text{ erg cm}^{-2}$.

Finally, we find the total burst fluence emitted during the burst storm, $F_{\text{tot}} = (5.0 \pm 0.1) \times 10^{-6} \text{ erg cm}^{-2}$ in the 0.5–10 keV energy range, which translates to a total energy emitted in the bursts of $4.8 \times 10^{40} \text{ erg}$. This measurement should be considered a lower limit because, for at least the brighter bursts, the spectral peak is at energy > 10 keV, beyond the coverage of NICER (Younes et al. 2020a).

3.4. Properties of Bursts Beyond the Burst Storm

The April 28 NICER observation exhibits five GTIs, of which the last four occur 2.9, 4.4, 5.8, and 15 hr after the first GTI (i.e., the burst storm; Figure 1). We find two bursts in each of GTIs 2, 3, and 4 and none in the very last. Given their similar exposure, we derive for each a burst rate of

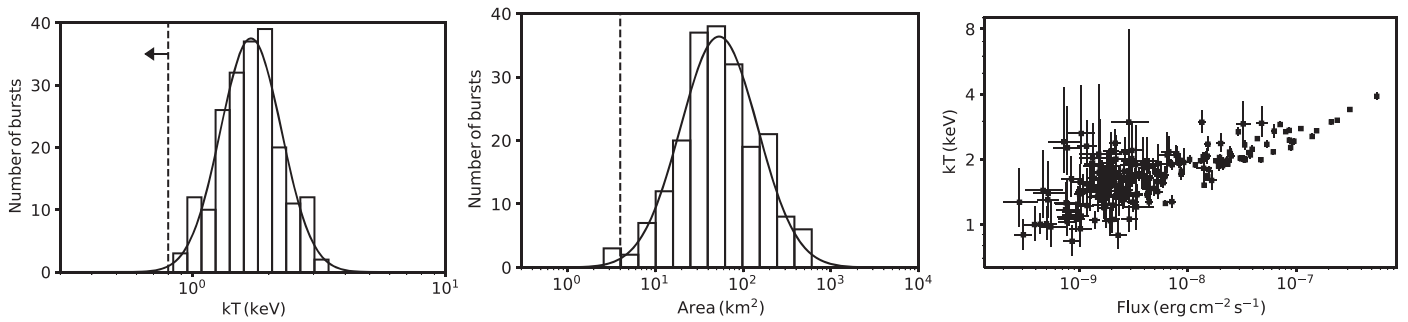


Figure 6. Left panel: distribution of the burst BB temperatures along with the best-fit lognormal function (solid line). The vertical dashed line is the highest BB temperature measured for the persistent emission. The arrow indicates the surface temperature evolution trend during the outburst decay. Middle panel: distribution of the burst BB area along with the best-fit lognormal function (solid line). The vertical dashed line is the BB area of the persistent emission. Right panel: burst BB temperature vs. flux, measured in the 0.5–10 keV energy band.

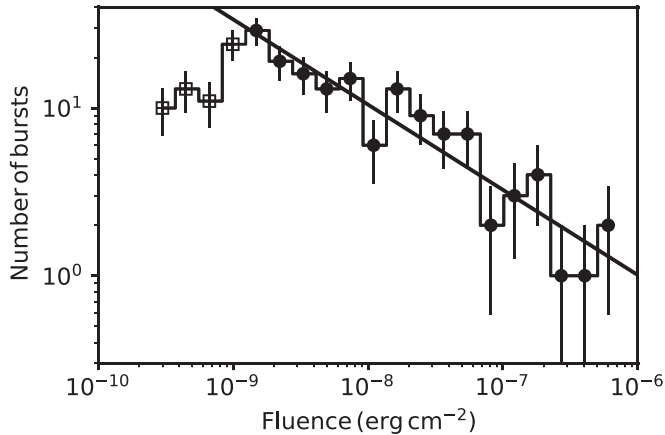


Figure 7. Burst fluence distribution of the bursts detected during the SGR 1935+2154 burst storm. The filled dots represent the bursts for which our detection efficiency is $\geq 99\%$. Open squares represent fluences with decreased detection efficiency. The solid line is a PL fit to the filled dots only, $N \propto F^{-0.5 \pm 0.1}$.

0.008 bursts s^{-1} . This is in contrast to the burst rate of >0.2 bursts s^{-1} we detect during the burst storm, just 3 hr earlier. The average T_{90} of these bursts is 0.6 s, roughly consistent with the average burst storm T_{90} . Their spectra are well fit with a BB model with temperatures also consistent with the bulk of the bursts detected during the burst storm. In contrast, the average fluence of these bursts is 4.5×10^{-10} erg cm^{-2} , which is only consistent with the very faint end of the fluence distribution shown in Figure 7.

4. Persistent Emission

4.1. Timing

We searched for the spin period of SGR 1935+2154 using the barycenter-corrected events detected during the first NICER observation, ID 3020560101, after excluding all identified bursts. To increase our sensitivity for period detection, we excluded the first GTI of the observation, since it is strongly contaminated by bursts that are not resolved from the underlying persistent emission (Section 3.3). We also only considered events in the energy range 1.5–5 keV, and we restricted our search interval to the period range $3.236 \text{ s} < P < 3.249 \text{ s}$, which encapsulates the source spin period, $P = 3.24731(1) \text{ s}$, as derived from NICER observations performed on April 29 and 30 (Borghese et al. 2020). We find the largest Z_1^2 (Bucccheri et al. 1983) power of 24.5 at a frequency $\nu = 0.307946(2)$ (the number in parentheses represents the 1σ uncertainty, which

corresponds to a change in Z_1^2 by 2.3). This corresponds to a period $P = 3.24732(2)$ at a reference time 58,967.423047 MJD. This period is consistent at the 1σ level with the one in Borghese et al. (2020), which implies a 3σ upper limit on any spin-down or spin-up event, $|\dot{P}| \gtrsim 6.0 \times 10^{-10} \text{ s s}^{-1}$. Figure 5 (top panel) shows the 1.5–5 keV pulse profile in black. We derive an rms pulse fraction of $8\% \pm 2\%$; however, we note that this value is not background-corrected and should be considered a lower limit.

The fast decay trend of the persistent emission flux beyond the first exposure resulted in very few counts detected in each separate observation for pulsation searches. However, NICER performed heavy cadence observations on two occasions during the outbursts, observing SGR 1935+2154 almost daily. The first (interval 1) covered days 21–39 from the outburst onset (ObsIDs 3020560105–3020560119), while the second (interval 2) extended from days 54 to 68 (ObsIDs 3020560120–3020560133). Hence, we searched simultaneously for the source spin frequency and its derivative, $0.3079 < \nu < 0.3080$ and $-12 < \log \dot{\nu} < -11$ in steps of $\Delta\nu/1000$ and $\Delta \log \dot{\nu}/500$, for each of these time spans using two different methods, the Z^2 test (Bucccheri et al. 1983) and an epoch-folding or χ^2 test (e.g., Staelin 1969).

During interval 1, the total NICER exposure is 24.3 ks, detecting about 17,800 counts in the energy range 1.5–5 keV. Both methods resulted in the detection of a strong signal, $Z^2 = 77$ and $\chi^2 = 91$, with spin parameters consistent at the 1σ level. We then refined this timing model through a phase-coherence analysis by dividing the interval into four portions, each with about 4500 counts. From the latter, we estimate the spin frequency $\nu = 0.30794014(1)$ and frequency derivative $\dot{\nu} = -3.72(3) \times 10^{-12} \text{ Hz s}^{-1}$ (reference time 58,997.571 MJD). The photon arrival times of interval 1 folded with the above timing model are shown in the bottom panel of Figure 5. We measure an rms pulsed fraction of $6.7\% \pm 0.8\%$. The dotted lines are the corresponding phases of the two radio bursts detected on 2020 May 24 (Kirsten et al. 2020).

The NICER exposure of SGR 1935+2154 during interval 2 is 21.5 ks, detecting a total of 12,100 counts in the energy range 1.5–5 keV. Applying the same methodology as above, we cannot detect significant pulsations within the searched $(\nu, \dot{\nu})$ range. We also tried to phase-connect intervals 1 and 2; however, we do not detect the source pulse in interval 2 when folding with the timing model derived for interval 1. Assuming a similar pulse shape compared to interval 1, we estimate a 3σ upper limit on the rms pulsed fraction of about 5%.

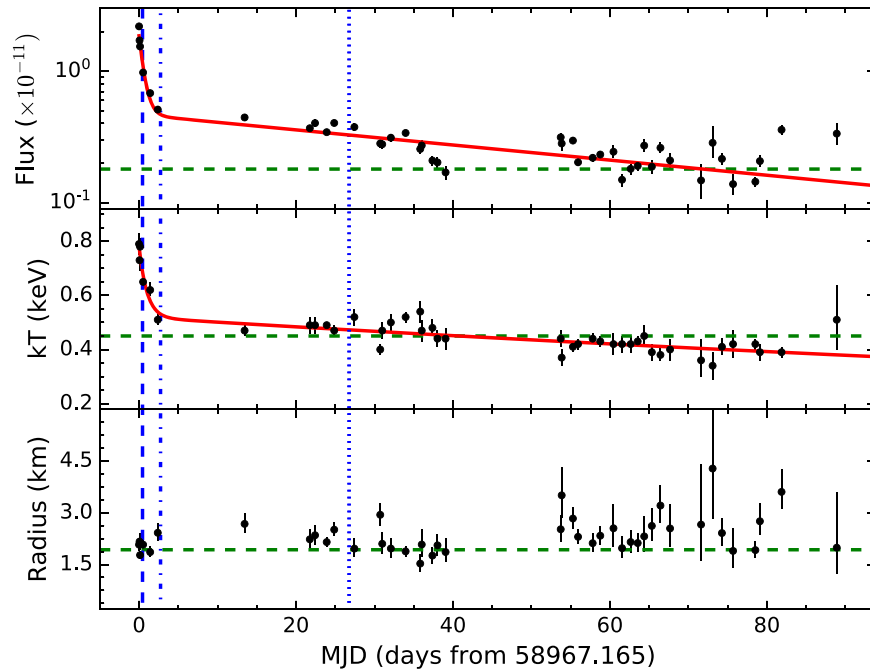


Figure 8. Spectral evolution of the persistent emission of SGR 1935+2154 observed with NICER after the initial observation obtained on 2020 April 28. From top to bottom, the panels show the evolution in the 0.3–10 keV range of the unabsorbed flux (in units of $\text{erg s}^{-1} \text{cm}^{-2}$), the BB temperature, and the emitting radius assuming a distance of 9 kpc. In all panels, green dashed lines show the average of the values inferred from historical NICER observations obtained in 2017–2019, before the source burst active period. The blue vertical dashed, dotted, and dashed–dotted lines, respectively, mark the times of the FRB-like event, two additional weak radio bursts (Kirsten et al. 2020), and another weak radio burst reported by FAST (Zhang et al. 2020) from the source. The red solid curves in the top two panels constitute the best-fit double exponential decay models to the flux and BB temperature, displaying an initial very rapid rise and then a much slower decline.

4.2. Spectroscopy

We perform spectral analysis on the persistent emission of SGR 1935+2154 starting with the second GTI of the first NICER observation (Figure 1). We exclude the first GTI due to strong contamination from unresolved burst emission. We fit the X-ray spectra in the energy range of 1.0–5.0 keV. The background starts to dominate beyond 5 keV due to the softness and relatively low flux of the source. In this energy range, the X-ray spectra are well described by an absorbed BB model. We fix the hydrogen column density to $2.4 \times 10^{22} \text{ cm}^{-2}$, which is inferred from earlier high-S/N Chandra and XMM-Newton data (Younes et al. 2017b). Our results are given in Table 1, and the spectral parameter evolution is shown in Figure 8. In the latter, we also show the average of the spectral parameters as obtained from earlier NICER observations of SGR 1935+2154 during 2017–2019.

5. Discussion

We have analyzed the NICER monitoring of SGR 1935+2154 following its most intense burst active period. We report on the statistical characteristics of 217 bursts detected in the first observation taken on 2020 April 28, 6 hr after the start of the latest activity episode of the source. We also report the timing and spectral analysis results of the persistent emission of the source on that day, as well as their spectral evolution up to 90 days after the outburst onset. In the following, we discuss our results in comparison to other magnetar burst storms and active episodes.

5.1. SGR 1935+2154 Burst Storm Comparison to Other Magnetars

On 2020 April 27, SGR 1935+2154 entered its sixth and most intense burst active episode, emitting tens of bright bursts

detected in the span of minutes. NICER started observing SGR 1935+2154 just 6 hr after the initial trigger and caught the tail end of the burst storm during a span of 1120 s, detecting bursts at a rate of $>0.2 \text{ bursts s}^{-1}$. Large burst rates have previously been observed from several magnetars, such as SGR 1900+14 (Göğüş et al. 1999; Israel et al. 2008), SGR 1806–20 (Woods et al. 2007), SGR 1627–41 (Woods et al. 1999b; Esposito et al. 2008), 1E 2259+586 (Gavriil et al. 2004), and SGR J1550–5418 (Mereghetti et al. 2009; Israel et al. 2010; Scholz & Kaspi 2011; van der Horst et al. 2012). We discuss below a qualitative comparison across magnetars, as a quantitative comparison is not feasible, given the different characteristics (e.g., energy ranges and sensitivity) of the instruments with which they were observed.

The average T_{90} duration of 840 ms for SGR 1935+2154 bursts is among the highest within the magnetar burst family (e.g., Collazzi et al. 2015). Yet most of the T_{90} values for other magnetars have come from large field-of-view, high-background instruments operating above 5 keV (e.g., CGRO-BATSE and Fermi-GBM) that may have skewed durations toward lower values (e.g., Israel et al. 2008; Younes et al. 2014). For instance, some of the bursts we report here were also detected with Fermi-GBM above 8 keV. It is quite evident by comparing the NICER and GBM light curves of these bursts that the latter misses the weak tails of the bursts and hence results in an underestimate of their T_{90} (see, e.g., Figure 1 in Younes et al. 2020a). Hence, our larger-than-usual T_{90} measurement is likely a reflection of the large sensitivity and low background of NICER rather than an indication of an intrinsic source property.

Regarding burst morphology, we find very few single-peaked bursts, with the majority showing multi-peaked profiles. Roughly 65% of our bursts have shorter rise than fall times,

commensurate with the bulk of magnetar bursts, especially the ones observed during burst storms (e.g., van der Horst et al. 2012). Notably, the average rise-to-fall time ratio of 0.69 we find for SGR 1935+2154 is quite similar to the 0.59 value measured for another prolific burster, 1E 1547.0–5408 (Scholz & Kaspi 2011). We note that we cannot exclude the possibility that some bursts in our sample are the superposition of two or more independent events, which may impact the results of our distributions somewhat.

The waiting-time distributions of magnetar bursts during burst storms have been documented for several magnetars. For instance, Göğüş et al. (1999) studied SGR 1900+14 bursts observed with RXTE during its 1998 burst storm, while Gavriil et al. (2004) studied the ones from 1E 2259+586 during its 2002 outburst. Both studies found that waiting times follow a lognormal distribution with a mean value of ~ 50 s. We find that the waiting times for the SGR 1935+2154 bursts also follow a lognormal distribution but with a mean of about $2.1_{-1.4}^{+5.2}$ s, albeit capturing the latter part of its burst storm. This marked difference could reflect a peculiar character of the SGR 1935+2154 storm, yet it could also be partly due to how the waiting times are determined. Gavriil et al. (2004) noted a positive correlation between the waiting time and the time of the next burst (from a fiducial start time) over their 10 ks exposure of 1E 2259+586. In fact, the average waiting time within the first 1 ks of their observation (comparable to the length of our burst storm observation) is about 10 s. The larger burst rate observed from SGR 1935+2154 during this burst storm relative to that for 1E 2259+586 may yield shorter waiting times, on average; this may be due in part to the intrinsic nature of the SGR 1935+2154 storm, yet it may also reflect the excellent sensitivity below 5 keV of the NICER detector. Interestingly, a lognormal waiting-time distribution has also been derived for the repeating FRB 121102 (Katz 2019; Wadiasingh & Timokhin 2019).

Several previous works have shown that magnetar burst fluences (and hence energies) follow a PL distribution $dN/dF \propto F^{-\alpha}$. This relation holds over several orders of magnitude in fluence ranging from $\sim 10^{-10}$ to 10^{-5} erg cm $^{-2}$ (e.g., Göğüş et al. 2000; Gavriil et al. 2004; Lin et al. 2013). For most magnetars, the index of this relation has been shown to cluster around -1.6 (e.g., Cheng et al. 1996; Göğüş et al. 1999, 2000; Aptekar et al. 2001; Gavriil et al. 2004; Scholz & Kaspi 2011; van der Horst et al. 2012; Lin et al. 2013). This is similar to the energy distribution shape of terrestrial earthquakes (e.g., Gutenberg & Richter 1956) and solar flares (e.g., Crosby et al. 1993), both of which result in an index of ~ -1.6 . The SGR 1935+2154 burst fluence distribution is also well modeled with a PL function with an index $\alpha = -1.5 \pm 0.1$, clearly commensurate with the values inferred for other magnetars. This suggests a universal property of the burst energetics for the whole magnetar class, perhaps underpinned by the phenomenon of self-organized criticality (Göğüş et al. 1999).

Magnetar burst spectra are best described with either a cutoff PL or a 2BB model, both of which result in a turnover in the 20–50 keV energy range (e.g., Enoto et al. 2012; Lin et al. 2012). Spectra of SGR 1935+2154 in the 8–200 keV range from the previous activations are well fit with both models, with spectral parameters broadly consistent with the rest of the magnetar family, albeit softer, on average, than some (Lin et al. 2020). During the 2020 burst storm, Younes et al. (2020a) presented the NICER +GBM spectral analysis of 24 bursts, also showing that they are

commensurate with the previous activations. These authors, as well as others (e.g., Ridnaia et al. 2020), found a positive correlation between the high-energy cutoff and the burst flux. This implies that, for most of the bursts we analyze here, the cutoff energy is around the few keV range, well within the NICER 1–10 keV energy band. This may explain why a simple PL cannot explain the spectra well, whereas a BB model, which mimics a cutoff PL in shape when restrained to small energy ranges, gives a good fit to the bulk of the bursts. However, the spectral analysis presented here is restricted to the NICER energy range, which is less sensitive above 5 keV, thus possibly imposing a bias in the burst spectral analysis.

Finally, the lack of dependency of the burst peak arrival times with phase is also consistent with the majority of magnetar sources (e.g., Scholz & Kaspi 2011); see also the literature survey in Elenbaas et al. (2018). This implies that magnetar bursts occur approximately randomly in magnetic colatitudes in the magnetosphere, perhaps close to the stellar surface. Yet the bursts are not spatially proximate to the surface locale of the persistent pulsed emission, though there may be a physical association between the transient and quiescent signals mediated by field line flux tubes in either dipolar or twisted field geometries.

5.2. Persistent Emission

Following strong bursting activity, the increase in the persistent X-ray flux level is ubiquitous in magnetars. This increase is often accompanied by hardening of the X-ray spectra, usually in the form of higher surface thermal temperature and/or a decrease in the PL index (e.g., Coti Zelati et al. 2018). These characteristics are evident in the case of the SGR 1935+2154 previous activations (Israel et al. 2016; Younes et al. 2017b), as well as the current one (Borghese et al. 2020). Younes et al. (2017b) noted that the SGR 1935+2154 persistent emission flux increased in proportion to the total energy emitted in the bursts, with the largest increase (by a factor of 7) detected following the 2016 bursting episode, the most intense up to that time. The initial flux increase of $\gtrsim 10$ during the 2020 bursting activity is consistent with the above picture.

The flux evolution during the previous episodes showed an initial rapid exponential decay with a characteristic timescale of a few days, possibly followed by a shallower return to quiescence. Our NICER monitoring of the 2020 activation also reveals two decay trends, which can be well characterized with a double exponential function, with very different e-folding times. As can be seen from Figure 8, SGR 1935+2154 shows an initial rapid decay with a best-fitting e-folding time of 0.65 ± 0.08 days, followed by a long-term flux decay and cooling whose e-folding time is 75 ± 5 days. The decay in flux is accompanied by cooling (middle panel of Figure 8). In fact, a similar double exponential decay model can be used to fit the decay in the inferred BB temperature. The best-fit parameters of such a model are two e-folding times of 0.99 ± 0.3 and 285 ± 45 days, respectively. On the other hand, the apparent emitting radius only exhibits a marginal increase with time with a slope of 0.46 ± 0.15 km per 100 days.

Such an initially rapid flux decrease followed by a more shallow decline has previously been observed from a few magnetars (e.g., An et al. 2012; Kargaltsev et al. 2012) and is indicative of cooling hot spots. These spots can develop at the onset of the outburst through either surface bombardment by relativistic particles that are energized in the magnetosphere by toroidal twists to the global field structure (Thompson et al. 2002; Beloborodov 2013; González-Caniulef et al. 2019) or an

internal seismic process such as crustal shearing induced by stresses imposed by the enormous fields (Thompson & Duncan 1996; Pons et al. 2009). This cooling picture is clearly demonstrated in the middle panel of Figure 8 and accompanied by a stability of the inferred radius of the emitting area (Figure 8, bottom). It is notable that after about 50 days, the spectral fitting yields systematically lower temperatures than the historical ones obtained in the 2017–2019 period that are indicated by the green dashed lines in Figure 8. Yet due to the lower flux of the source and the known degeneracy between the emitting area and the temperature of the BB model, the uncertainties in these determinations are relatively high.

The source broad double-peaked pulse shape in the soft X-ray band (Figure 5; see also Borghese et al. 2020) differs markedly from the single-peaked, quasi-sinusoidal pulse profile following its 2014 outburst (Israel et al. 2016), implying that distinct regions are heated on the surface of the star during each outburst. We also detect clear evolution in the pulse profile during this outburst; the prominent peak led the secondary one immediately after outburst onset (see also Borghese et al. 2020) but flipped 20 days later. Such pulse shape evolution during outburst epochs is rather common to magnetars (e.g., Woods et al. 1999a; Göğüş et al. 2002; Esposito et al. 2010; Ng et al. 2011; Rodríguez Castillo et al. 2014, 2016; Younes et al. 2015), possibly pointing to a complex magnetic field topology. For SGR 1935+2154, the separation by ~ 0.3 in phase of the two peaks provides evidence in favor of this assertion.

Finally, the spin-down rate that we measure between days 21 and 39 postoutburst is a factor of 2.7 larger than the rate measured in 2014 ($\dot{\nu} = -1.36 \times 10^{-12} \text{ Hz s}^{-1}$; Israel et al. 2016), indicating a larger torque on the magnetar. This is yet another distinct characteristic of magnetar in outburst (e.g., Woods et al. 2007), which is believed to emanate from increased particle wind in the magnetosphere due to the strong bursting activity (Harding et al. 1999; Tong et al. 2013).

5.3. The FRB Connection

The pulse period detection of SGR 1935+2154 during the first NICER observation, which brackets the time of the FRB (see Figure 1), enabled us to place it—and, by extension, the peak of the X-ray-associated burst—on the pulse profile; this is a crucial piece of information that has not been achieved before. Figure 7 demonstrates that the FRB time aligns with the principal peak of the pulse profile. It is common in the magnetar literature to attribute the peak to an observer viewing a hot region on the neutron star surface (e.g., Perna & Gotthelf 2008; Albano et al. 2010; Younes et al. 2020b). If the heating originates internally, the hot spot would naturally be associated with the magnetic poles, since heat conduction upward from the crust is efficient when the field is oriented vertically. As an alternative possibility, twists in magnetic field loops can lead to the development of surface hot spots via particle bombardment, discussed in Section 5.2. Such twists can also favor quasi-polar hot spots or annuli, since stresses in the crust that drive twists are generally larger in polar regions (e.g., Perna & Pons 2011). In either scenario, the pulse peak for SGR 1935+2154 can then be realized if the magnetar is instantaneously viewed almost down the polar axis, thereby concluding that the FRB is somehow intimately connected to the polar field lines. Yet we remark that nonpolar surface hot-spot locales can also be entertained.

This special observational perspective is in fact the picture that was drawn by Younes et al. (2020a) via a comparison of the broadband spectroscopic signal of NICER+Fermi-GBM bursts and the FRB-associated burst as observed with HXMT (Li et al. 2020). This scenario of an ephemeral (due to stellar rotation) polar viewing of the FRB and its contemporaneous, spectroscopically unique X-ray burst could help explain the rarity of both and restricts the range of possible viewing and rotational geometries for SGR 1935+2154.











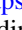




A physical connection between the surface pole and a radio emission zone has a precedent in canonical, young/middle-aged radio pulsars, which also exhibit phase-aligned persistent radio and surface thermal X-ray signals. In those systems, global magnetospheric solutions (e.g., Contopoulos et al. 1999; Bai & Spitkovsky 2010; Kalapotharakos et al. 2014) require pair cascades that both generate return currents that bombard and heat polar cap zones (Harding & Muslimov 2001; Timokhin & Arons 2013) and seed coherent radio emission (Philippov et al. 2020). Yet magnetar magnetospheres differ profoundly from those of pulsars, with their currents generally being associated with twisted field geometries in closed field zones (Thompson et al. 2002; Chen & Beloborodov 2017). Moreover, much of the magnetar activity associated with such twists is ephemeral. The ability here to determine the X-ray pulse phase associated with the FRB provides an important advance toward understanding the FRB–magnetar connection, with potential implications for the extragalactic FRB paradigm.

We find that the two fainter radio bursts detected by Kirsten et al. (2020), which were separated by 1.4 s, are offset from the X-ray pulse peaks. As pointed out by those authors, it is not yet clear what the origin of such radio bursts is, whether they are driven by similar physical and emission mechanisms that resulted in the FRB or different ones. Interestingly, three more radio bursts with comparable fluence have recently been detected from SGR 1935+2154 during a single rotational period with a peak separation of 0.95 s between the first and second and 1.95 s between the second and third bursts (Pleunis & CHIME/FRB Collaboration 2020). This indicates that these radio bursts are likely occurring sporadically at largely distinct phases. This is unlike the more persistent radio magnetar emission that mostly clusters in a small rotational phase space (e.g., XTEJ1810–197; Maan et al. 2019; and now perhaps SGR 1935+2154; Zhu et al. 2020). Assuming that repeating FRBs are produced in the close environs of magnetars, the above result fits with the fact that no magnetar-like periodic behavior has so far been detected from these sources (e.g., Zhang et al. 2018).

A portion of this work was supported by NASA through the NICER mission and the Astrophysics Explorers Program. This research has made use of data and software provided by the High Energy Astrophysics Science Archive Research Center (HEASARC), which is a service of the Astrophysics Science Division at NASA/GSFC and the High Energy Astrophysics Division of the Smithsonian Astrophysical Observatory. The authors are grateful to the referee for constructive comments that improved the quality of the manuscript. G.Y. sincerely thanks Jason Hessels for his request to perform more detailed late-time temporal analysis, which proved highly fruitful. G.Y. acknowledges support from NASA under NICER Guest Observer cycle 1 program 2098, grant No. 80NSSC19K1452. M.G.B. acknowledges the generous support of the National

Science Foundation through grant AST-1813649. Z.W. is supported by the NASA postdoctoral program. C.K. acknowledges support from NASA under grant 80NSSC17K0761. This work has made use of the NASA Astrophysics Data System.

ORCID iDs



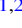











George Younes  <https://orcid.org/0000-0002-7991-028X>
 Tolga Güver  <https://orcid.org/0000-0002-3531-9842>
 Chryssa Kouveliotou  <https://orcid.org/0000-0003-1443-593X>
 Matthew G. Baring  <https://orcid.org/0000-0003-4433-1365>
 Chin-Ping Hu  <https://orcid.org/0000-0001-8551-2002>
 Zorawar Wadiasingh  <https://orcid.org/0000-0002-9249-0515>
 Beste Begičarslan  <https://orcid.org/0000-0001-5072-8444>
 Teruaki Enoto  <https://orcid.org/0000-0003-1244-3100>
 Ersin Göğüş  <https://orcid.org/0000-0002-5274-6790>
 Lin Lin  <https://orcid.org/0000-0002-0633-5325>
 Alice K. Harding  <https://orcid.org/0000-0001-6119-859X>
 Alexander J. van der Horst  <https://orcid.org/0000-0001-9149-6707>
 Walid A. Majid  <https://orcid.org/0000-0002-4694-4221>
 Sebastien Guillot  <https://orcid.org/0000-0002-6449-106X>
 Christian Malacaria  <https://orcid.org/0000-0002-0380-0041>

References

- Albano, A., Turolla, R., Israel, G. L., et al. 2010, *ApJ*, 722, 788
 An, H., Archibald, R. F., Hascoët, R., et al. 2015, *ApJ*, 807, 93
 An, H., Kaspi, V. M., Tomsick, J. A., et al. 2012, *ApJ*, 757, 68
 Aptekar, R. L., Frederiks, D. D., Golenetskii, S. V., et al. 2001, *ApJS*, 137, 227
 Arnaud, K. A. 1996, in ASP Conf. Ser. 101, *Astronomical Data Analysis Software and Systems V*, ed. G. H. Jacoby & J. Barnes (San Francisco, CA: ASP), 17
 Bai, X.-N., & Spitkovsky, A. 2010, *ApJ*, 715, 1282
 Barthelmy, S. D., Bernardini, M. G., D’Avanzo, P., et al. 2020, GCN, 27657, 1
 Beloborodov, A. M. 2013, *ApJ*, 762, 13
 Bochenek, C. D., Ravi, V., Belov, K. V., et al. 2020, *Natur*, 587, 59
 Borghese, A., Coti Zelati, F., Rea, N., et al. 2020, *ApJL*, 902, L2
 Buccheri, R., Bennett, K., Bignami, G. F., et al. 1983, *A&A*, 128, 245
 Chen, A. Y., & Beloborodov, A. M. 2017, *ApJ*, 844, 133
 Cheng, B., Epstein, R. I., Guyer, R. A., & Young, A. C. 1996, *Natur*, 382, 518
 Collazzi, A. C., Kouveliotou, C., van der Horst, A. J., et al. 2015, *ApJS*, 218, 11
 Contopoulos, I., Kazanas, D., & Fendt, C. 1999, *ApJ*, 511, 351
 Coti Zelati, F., Rea, N., Pons, J. A., Campana, S., & Esposito, P. 2018, *MNRAS*, 474, 961
 Crosby, N. B., Aschwanden, M. J., & Dennis, B. R. 1993, *SoPh*, 143, 275
 Eilers, P. H., & Boelens, H. F. 2005, Leiden University Medical Centre Report, 1, 5
 Elenbaas, C., Watts, A. L., & Huppenkothen, D. 2018, *MNRAS*, 476, 1271
 Enoto, T., Nakagawa, Y. E., Sakamoto, T., & Makishima, K. 2012, *MNRAS*, 427, 2824
 Esposito, P., Israel, G. L., Turolla, R., et al. 2010, *MNRAS*, 405, 1787
 Esposito, P., Israel, G. L., Zane, S., et al. 2008, *MNRAS*, 390, L34
 Fletcher, C., & Fermi GBM Team 2020, GCN, 27659, 1
 Gavriil, F. P., Kaspi, V. M., & Woods, P. M. 2004, *ApJ*, 607, 959
 Gendreau, K. C., Arzoumanian, Z., Adkins, P. W., et al. 2016, *Proc. SPIE*, 9905, 99051H
 González-Caniulef, D., Zane, S., Turolla, R., & Wu, K. 2019, *MNRAS*, 483, 599
 Good, D., & CHIME/FRB Collaboration 2020, ATel, 14074, 1
 Göğüş, E., Woods, P. M., Kouveliotou, C., et al. 1999, *ApJL*, 526, L93
 Göğüş, E., Woods, P. M., Kouveliotou, C., et al. 2000, *ApJL*, 532, L121
 Göğüş, E., Kouveliotou, C., Woods, P. M., Finger, M. H., & van der Klis, M. 2002, *ApJ*, 577, 929
 Gutenberg, B., & Richter, C. F. 1956, *BuSSA*, 46, 105
 Harding, A. K., Contopoulos, I., & Kazanas, D. 1999, *ApJL*, 525, L125
 Harding, A. K., & Muslimov, A. G. 2001, *ApJ*, 556, 987
 Hurley, K., Cline, T., Mazets, E., et al. 1999, *Natur*, 397, 41
 Israel, G. L., Esposito, P., Rea, N., et al. 2010, *MNRAS*, 408, 1387
 Israel, G. L., Esposito, P., Rea, N., et al. 2016, *MNRAS*, 457, 3448
 Israel, G. L., Romano, P., Mangano, V., et al. 2008, *ApJ*, 685, 1114
 Kalapotharakos, C., Harding, A. K., & Kazanas, D. 2014, *ApJ*, 793, 97
 Kargaltsev, O., Kouveliotou, C., Pavlov, G. G., et al. 2012, *ApJ*, 748, 26
 Kaspi, V. M., & Beloborodov, A. M. 2017, *ARA&A*, 55, 261
 Katz, J. I. 2019, *MNRAS*, 487, 491
 Kirsten, F., Snelders, M., Jenkins, M., et al. 2020, *NatAs*, in press, (doi:10.1038/s41550-020-01246-3)
 Kothes, R., Sun, X., Gaensler, B., & Reich, W. 2018, *ApJ*, 852, 54
 Kouveliotou, C., Dieters, S., Strohmayer, T., et al. 1998, *Natur*, 393, 235
 Kouveliotou, C., Meegan, C. A., Fishman, G. J., et al. 1993, *ApJL*, 413, L101
 Li, C. K., Lin, L., Xiong, S. L., et al. 2020, arXiv:2005.11071
 Lin, L., Göğüş, E., Baring, M. G., et al. 2012, *ApJ*, 756, 54
 Lin, L., Göğüş, E., Roberts, O. J., et al. 2020, *ApJ*, 893, 156
 Lin, L., Göğüş, E., Kaneko, Y., & Kouveliotou, C. 2013, *ApJ*, 778, 105
 Luo, J., Ransom, S., Demorest, P., et al. 2019, PINT: High-precision pulsar timing analysis package, Astrophysics Source Code Library, ascl:1902.007
 Maan, Y., Joshi, B. C., Surnis, M. P., et al. 2019, *ApJL*, 882, L9
 Mazets, E. P., Golentskii, S. V., Ilinskii, V. N., Aptekar, R. L., & Guryan, I. A. 1979, *Natur*, 282, 587
 Mereghetti, S., Götz, D., Weidenspointner, G., et al. 2009, *ApJL*, 696, L74
 Mereghetti, S., Savchenko, V., Ferrigno, C., et al. 2020, *ApJL*, 898, L29
 Ng, C.-Y., Kaspi, V. M., Dib, R., et al. 2011, *ApJ*, 729, 131
 Palmer, D. M. 2020, ATel, 13675, 1
 Palmer, D. M., Barthelmy, S., Gehrels, N., et al. 2005, *Natur*, 434, 1107
 Perna, R., & Gotthelf, E. V. 2008, *ApJ*, 681, 522
 Perna, R., & Pons, J. A. 2011, *ApJL*, 727, L51
 Philippov, A., Timokhin, A., & Spitkovsky, A. 2020, *PhRvL*, 124, 245101
 Pleunis, Z., & CHIME/FRB Collaboration 2020, ATel, 14080, 1
 Pons, J. A., Miralles, J. A., & Geppert, U. 2009, *A&A*, 496, 207
 Rea, N., Israel, G. L., Pons, J. A., et al. 2013, *ApJ*, 770, 65
 Ridnaia, A., Svinikin, D., Frederiks, D., et al. 2020, arXiv:2005.11178
 Rodríguez Castillo, G. A., Israel, G. L., Esposito, P., et al. 2014, *MNRAS*, 441, 1305
 Rodríguez Castillo, G. A., Israel, G. L., Tiengo, A., et al. 2016, *MNRAS*, 456, 4145
 Scholz, P., & Kaspi, V. M. 2011, *ApJ*, 739, 94
 Scholz, P., Kaspi, V. M., & Cumming, A. 2014, *ApJ*, 786, 62
 Staelin, D. H. 1969, *IEEEP*, 57, 724
 Stamatikos, M., Malesani, D., Page, K. L., & Sakamoto, T. 2014, GCN, 16520, 1
 Tavani, M., Casentini, C., Ursi, A., et al. 2020, arXiv:2005.12164
 The CHIME/FRB Collaboration, Andersen, B. C., et al. 2020, *Natur*, 587, 54
 Thompson, C., & Duncan, R. C. 1996, *ApJ*, 473, 322
 Thompson, C., Lyutikov, M., & Kulkarni, S. R. 2002, *ApJ*, 574, 332
 Timokhin, A. N., & Arons, J. 2013, *MNRAS*, 429, 20
 Tong, H., Xu, R. X., Song, L. M., et al. 2013, *ApJ*, 768, 144
 Turolla, R., Zane, S., & Watts, A. L. 2015, *RPPH*, 78, 116901
 van der Horst, A. J., Kouveliotou, C., Gorgone, N. M., et al. 2012, *ApJ*, 749, 122
 Verner, D. A., Ferland, G. J., Korista, K. T., & Yakovlev, D. G. 1996, *ApJ*, 465, 487
 Wadiasingh, Z., & Timokhin, A. 2019, *ApJ*, 879, 4
 Wilms, J., Allen, A., & McCray, R. 2000, *ApJ*, 542, 914
 Woods, P. M., Kaspi, V. M., Thompson, C., et al. 2004, *ApJ*, 605, 378
 Woods, P. M., Kouveliotou, C., Finger, M. H., et al. 2007, *ApJ*, 654, 470
 Woods, P. M., Kouveliotou, C., van Paradijs, J., et al. 1999a, *ApJL*, 524, L55
 Woods, P. M., Kouveliotou, C., van Paradijs, J., et al. 1999b, *ApJL*, 519, L139
 Younes, G., Baring, M. G., Kouveliotou, C., et al. 2017a, *ApJ*, 851, 17
 Younes, G., Baring, M. G., Kouveliotou, C., et al. 2020a, arXiv:2006.11358
 Younes, G., Baring, M. G., Kouveliotou, C., et al. 2020b, *ApJL*, 889, L27
 Younes, G., Guver, T., Enoto, T., et al. 2020c, ATel, 13678, 1
 Younes, G., Kouveliotou, C., Jaodand, A., et al. 2017b, *ApJ*, 847, 85
 Younes, G., Kouveliotou, C., & Kaspi, V. M. 2015, *ApJ*, 809, 165
 Younes, G., Kouveliotou, C., van der Horst, A. J., et al. 2014, *ApJ*, 785, 52
 Zhang, C. F., Jiang, J. C., Men, Y. P., et al. 2020, ATel, 13699, 1
 Zhang, Y. G., Gajjar, V., Foster, G., et al. 2018, *ApJ*, 866, 149
 Zhong, S.-Q., Dai, Z.-G., Zhang, H.-M., et al. 2020, *ApJL*, 898, L5
 Zhou, P., Zhou, X., Chen, Y., et al. 2020, arXiv:2005.03517
 Zhu, W., Wang, B., Zhou, D., et al. 2020, ATel, 14084, 1



Erratum: “NICER View of the 2020 Burst Storm and Persistent Emission of SGR 1935+2154” (2020, ApJL, 904, L21)

George Younes^{1,2} , Tolga Güver^{3,4} , Chryssa Kouveliotou^{1,2} , Matthew G. Baring⁵ , Chin-Ping Hu⁶ , Zorawar Wadiasingh⁷ , Beste Begičarslan³, Teruaki Enoto⁸ , Ersin Göğüş⁹ , Lin Lin¹⁰ , Alice K. Harding⁷ , Alexander J. van der Horst^{1,2} , Walid A. Majid^{11,12} , Sebastien Guillot¹³ , and Christian Malacaria^{14,15} 

¹ Department of Physics, The George Washington University, Washington, DC 20052, USA; gyounes@gwu.edu

² Astronomy, Physics and Statistics Institute of Sciences (APSYS), The George Washington University, Washington, DC 20052, USA

³ Istanbul University, Science Faculty, Department of Astronomy and Space Sciences, Beyazıt, 34119, Istanbul, Turkey

⁴ Istanbul University Observatory Research and Application Center, Istanbul University 34119, Istanbul, Turkey

⁵ Department of Physics and Astronomy, Rice University, MS-108, P.O. Box 1892, Houston, TX 77251, USA

⁶ Department of Physics, National Changhua University of Education, Changhua 50007, Taiwan

⁷ Astrophysics Science Division, NASA Goddard Space Flight Center, Greenbelt, MD 20771, USA

⁸ Extreme Natural Phenomena RIKEN Hakubi Research Team, Cluster for Pioneering Research, RIKEN, 2-1 Hirosawa, Wako, Saitama 351-0198, Japan

⁹ Sabanci University, Faculty of Engineering and Natural Sciences, Istanbul 34956, Turkey

¹⁰ Department of Astronomy, Beijing Normal University, Beijing 100875, People’s Republic of China

¹¹ Jet Propulsion Laboratory, California Institute of Technology, Pasadena, CA 91109, USA

¹² California Institute of Technology, Pasadena, CA 91125, USA

¹³ IRAP, CNRS, 9 avenue du Colonel Roche, BP 44346, F-31028 Toulouse Cedex 4, France

¹⁴ NASA Marshall Space Flight Center, NSSTC, 320 Sparkman Drive, Huntsville, AL 35805, USA

¹⁵ Universities Space Research Association, Science and Technology Institute, 320 Sparkman Drive, Huntsville, AL 35805, USA

Received 2021 May 1; published 2021 May 25

We have been made aware that the arrival times of the SGR J1935+2154 radio bursts presented in Table 2 of Kirsten et al. (2021) are in the Coordinated Universal Time (UTC) system, corrected to the solar system barycenter (Kirsten et al. 2021). Unfortunately in Younes et al. (2020), we assumed that the radio burst times were given in Terrestrial Dynamical Time (TDT or TT), corrected to the solar system barycenter, i.e., in Barycentric Dynamical Time (TDB). Since we used the latter time system to obtain the SGR J1935+2154 spin ephemerides (Section 4.1 in Younes et al. 2020), deriving the phases of the radio bursts using the times as presented in Kirsten et al. (2021) is erroneous (Younes et al. 2020, dotted blue lines in bottom panel of Figure 5).

The radio burst arrival times in the TDB system is 58993.93088958 and 58993.93090573 Modified Julian Day for B1 and B2, respectively (Kirsten et al. 2021; Kirsten et al. 2021). The correct rotational phases of the two bursts as compared to the X-ray pulse is shown in the corrected bottom panel of Figure 5. This figure supersedes the bottom panel of Figure 5 in Younes et al. (2020). Given that the two bursts still occur away from the peaks of the X-ray pulse, our conclusions in Section 5.3 are unaffected. Moreover, this correction does not affect any other element of the paper.

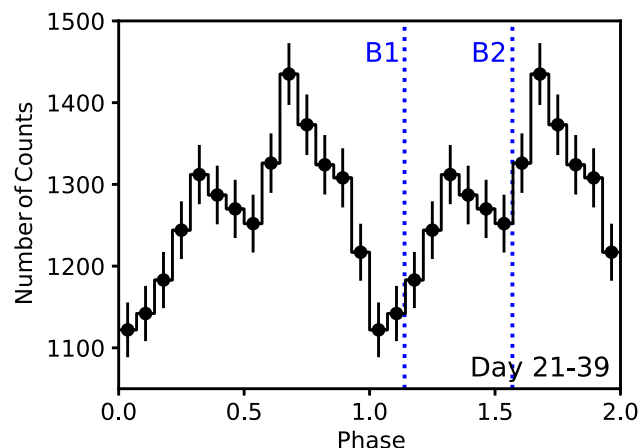










Figure 5. Pulse profile of the SGR J1935+2154 persistent emission as observed during days 21–39 post 2020 outburst. The dotted lines are the (now corrected) phases of the two radio bursts observed by Kirsten et al. (2021). This figure supersedes the bottom panel of Figure 5 in Younes et al. (2020). This correction does not affect any of our conclusions.

ORCID iDs

George Younes  <https://orcid.org/0000-0002-7991-028X>
Tolga Güver  <https://orcid.org/0000-0002-3531-9842>
Chryssa Kouveliotou  <https://orcid.org/0000-0003-1443-593X>
Matthew G. Baring  <https://orcid.org/0000-0003-4433-1365>
Chin-Ping Hu  <https://orcid.org/0000-0001-8551-2002>
Zorawar Wadiasingh  <https://orcid.org/0000-0002-9249-0515>
Teruaki Enoto  <https://orcid.org/0000-0003-1244-3100>
Ersin Göğüş  <https://orcid.org/0000-0002-5274-6790>

Lin Lin  <https://orcid.org/0000-0002-0633-5325>
Alice K. Harding  <https://orcid.org/0000-0001-6119-859X>
Alexander J. van der Horst  <https://orcid.org/0000-0001-9149-6707>
Walid A. Majid  <https://orcid.org/0000-0002-4694-4221>
Sebastien Guillot  <https://orcid.org/0000-0002-6449-106X>
Christian Malacaria  <https://orcid.org/0000-0002-0380-0041>

References

Kirsten, F., Snelders, M. P., Jenkins, M., et al. 2021, *NatAs*, 5, 414
Younes, G., Güver, G., Kouveliotou, C., et al. 2020, *ApJL*, 904, L21